NASA TECHNICAL NOTE

NASA TN D-8520

NASA TN D-8520

RANDOM AND SYSTEMATIC MEASUREMENT ERRORS IN ACOUSTIC IMPEDANCE AS DETERMINED BY THE TRANSMISSION LINE METHOD

Tony L. Parrott and C. D. Smith

Langley Research Center
Hampton, Va. 23665

1. Report No. NASA TN D-8520	2. Government Accession No.	3. Recipient's Catalog No.
4. Title and Subtitle RANDOM AND SYSTEMATIC MEASUREMENT ERRORS IN ACOUSTIC IMPEDANCE AS DETERMINED BY THE TRANSMISSION LINE METHOD		5. Report Date December 1977
		6. Performing Organization Code
7. Author(s) Tony L. Parrott and C. D. Smith		8. Performing Organization Report No. L-11231
9. Performing Organization Name and Address NASA Langley Research Center Hampton, VA 23665		10. Work Unit No. 505-03-11-04
		11. Contract or Grant No.
12. Sponsoring Agency Name and Address National Aeronautics and Space Administration Washington, DC 20546		13. Type of Report and Period Covered Technical Note
		14. Sponsoring Agency Code

15. Supplementary Notes

Tony L. Parrott: Langley Research Center.

C. D. Smith: The George Washington University.

16. Abstract

 The effect of random and systematic errors associated with the measurement of normal incidence acoustic impedance in a zero-mean-flow environment has been investigated by the transmission line method. The investigation was both experimental and analytical. The influence of random measurement errors in the reflection coefficients and pressure minima positions was investigated by computing fractional standard deviations of the normalized impedance. Both the standard techniques of random process theory and a simplified technique were used.

 Over a wavelength range of 68 to 10 cm (frequency range, 0.5 to 3.5 kHz), random measurement errors in the reflection coefficients and pressure minima positions could be described adequately by normal probability distributions with standard deviations of 0.001 and 0.0098 cm, respectively. The assumption of normal probability distributions for the measurement errors simplified the application of standard techniques in the calculation of standard deviations in the impedance components. An error propagation technique based on the observed concentration of the probability density functions was found to give essentially the same results but with a computation time of about 1 percent of that required for the standard technique.

 The results suggest that careful experimental design reduces the effect of random measurement errors to insignificant levels for moderate ranges of test specimen impedance component magnitudes. Most of the observed random scatter can be attributed to lack of control by the mounting arrangement over mechanical boundary conditions of the test sample.

17. Key Words (Suggested by Author(s)) Impedance measurements Acoustic impedance measurements	18. Distribution Statement Unclassified – Unlimited Subject Category 71
19. Security Classif. (of this report) Unclassified	20. Security Classif. (of this page) Unclassified	21. No. of Pages 71	22. Price* $5.25

RANDOM AND SYSTEMATIC MEASUREMENT ERRORS
IN ACOUSTIC IMPEDANCE AS DETERMINED
BY THE TRANSMISSION LINE METHOD

Tony L. Parrott and C. D. Smith[*]
Langley Research Center

SUMMARY

The effect of random and systematic errors associated with the measurement of normal incidence acoustic impedance in a zero-mean-flow environment has been investigated by the transmission line method. The investigation was both experimental and analytical. The influence of random measurement errors in the reflection coefficients and pressure minima positions was investigated by computing fractional standard deviations of the normalized impedance. Both the standard techniques of random process theory and a simplified technique were used.

Over a wavelength range of 68 to 10 cm (frequency range, 0.5 to 3.5 kHz), random measurement errors in the reflection coefficients and pressure minima positions could be described adequately by normal probability distributions with standard deviations of 0.001 and 0.0098 cm, respectively. The assumption of normal probability distributions for the measurement errors simplified the application of standard techniques in the calculation of standard deviations in the impedance components. An error propagation technique based on the observed concentration of the probability density functions was found to give essentially the same results but with a computation time of about 1 percent of that required for the standard technique.

The results suggest that careful experimental design reduces the effect of random measurement errors to insignificant levels for moderate ranges of test specimen impedance component magnitudes. Most of the observed random scatter can be attributed to lack of control by the mounting arrangement over mechanical boundary conditions of the test specimen.

INTRODUCTION

Measurements of normal incidence specific acoustic impedance continue to be important in determining the acoustic properties of materials considered for use in

---

[*]The George Washington University.

noise control. For materials that can be classed as locally reacting, the normal incidence impedance can specify the boundary condition in any system amenable to analysis. For homogeneous and isotropic materials characterized by extended reaction, two sets of normal incidence impedance measurements are sufficient to determine the material propagation constant and characteristic impedance. (See ref. 1.) Recent investigations dealing with the optimum design of noise-attenuating lined ducts (ref. 2) have raised questions about the degree of precision and accuracy needed to specify duct liner impedances. Reference 3 gives in situ impedance measurements on a duct liner at 20 axial locations 2.54 cm apart. These measurements indicated as much as a 30-percent random scatter about the mean trend. A limited error analysis suggested that the observed scatter was dominated by material inhomogeneity rather than by impedance measurement errors; however, a detailed discussion of the effects of random measurement errors was not given.

This investigation isolated the effects of measurement errors in the determination of acoustic impedance apart from the effects of material inhomogeneity. The investigation was limited to thin face-sheet materials studied in a zero-mean-flow environment by means of the transmission line method. Three different test specimens (designated A, B, and C) were used in the investigation. Specimen A was chosen because its impedance could be predicted theoretically. Therefore, a comparison of the theoretical and measured impedance for specimen A allowed the combined effect of all systematic errors to be evaluated. Test specimens B and C were fabricated from fiber metal. Repetitive measurements on all the specimens over the frequency range of 0.5 to 3.5 kHz in 0.1-kHz increments provided sufficient data to establish meaningful statistics for random variations in the measured reflection coefficients and pressure minima positions.

Two methods were used to calculate the standard deviations in the deduced test specimen impedance from the statistics of the measurements. In one method the standard techniques of stochastic process theory (hereafter called the exact method) were used to calculate the variances of the impedance components in terms of the functional relation between the impedance and the directly measured quantities. The second method (hereafter called the approximate method) resulted from a series expansion of the functional relation connecting impedance and the directly measured quantities. The resulting approximate formulas involved the first-order derivatives of the impedance components with respect to the measured quantities and their variances.

SYMBOLS

$A \qquad = \sum_{i=1}^{N} n_i^2$, cm^0, or $\sum_{i=1}^{N} x_i^2$, cm^2

A_1 amplitude of acoustic wave incident on test specimen, dynes-cm^{-2}

A_2 amplitude of acoustic wave transmitted through test specimen, dynes-cm^{-2}

B $= \displaystyle\sum_{i=1}^{N} n_i,\ cm^0,\ or\ \sum_{i=1}^{N} x_i,\ cm$

B_1 amplitude of acoustic wave reflected from test specimen, dynes-cm^{-2}

B_2 amplitude of acoustic wave reflected from cavity back, dynes-cm^{-2}

c sound speed at temperature T, cm-sec^{-1}

c_0 sound speed at reference temperature T_0, cm-sec^{-1}

c_p specific heat of air at constant pressure, cal-g^{-1}-$^{\circ}$C^{-1}

F_1, F_2 error propagation functions

f frequency, Hz

$f_{x_i}(x_i)$ probability density function for random variable x_i

$f_{\hat{x}_1}(\hat{x}_1)$ probability density function for random variable $\hat{x}_1$

$f_{R_i}(R_i)$ probability density function for random variable R_i

$f_{\hat{R}_0}(\hat{R}_0)$ probability density function for random variable $\hat{R}_0$

$f_{\hat{\lambda}}(\hat{\lambda})$ probability density function for random variable $\hat{\lambda}$

$J_0(\ )$ zeroth-order Bessel function

$J_2(\ )$ second-order Bessel function

j imaginary unit $\sqrt{-1}$

k wave number, $2\pi/\lambda$, cm^{-1}

l	channel length, cm
M	arbitrary integer
N	total number of pressure minima
n	complex polytropic gas constant
n_i	ith pressure minimum
P	porosity
p_{max}	maximum acoustic pressure, dynes-cm^{-2}
p_{min}	minimum acoustic pressure, dynes-cm^{-2}
R	specific acoustic resistance, g-cm^{-2}-sec^{-1}
R_i	reflection coefficient at ith pressure minimum
R_0	reflection coefficient at test specimen surface
r	radial coordinate, cm
r_c	channel radius (test specimen A), cm
r_p	probe radius, cm
r_0	reciprocal of reflection coefficient
S_i	standing-wave ratio associated with ith pressure minimum, dB
S_0	standing-wave ratio at specimen surface, dB
s	shear wave number, $r_c\sqrt{\dfrac{\rho\omega}{\mu_1}}$

T	working temperature, $^\circ$C
T_0	reference temperature, $^\circ$C
X	specific acoustic reactance, $g\text{-}cm^{-2}\text{-}sec^{-1}$
x	tube axial coordinate, cm
x_b	backing cavity depth, cm
x_i	position of ith pressure minimum relative to test specimen surface, cm
Z	specific acoustic impedance at test specimen surface, $g\text{-}cm^{-2}\text{-}sec^{-1}$
Z_b	specific impedance of backing cavity, $g\text{-}cm^{-2}\text{-}sec^{-1}$
Z_c	complex characteristic impedance of test specimen channel, $g\text{-}cm^{-2}\text{-}sec^{-1}$
α	tube-wall absorption coefficient, cm^{-1}
β	square root of Prandtl number, $\sqrt{\dfrac{\mu_1 c_p}{\kappa_1}}$
Γ	complex propagation constant for single channel of test specimen A, cm^{-1}
γ	ratio of specific heats for air
ζ	specific acoustic impedance ratio, $Z/\rho c$
η	nondimensional radial coordinate, r/r_c
θ	acoustic resistance ratio, $R/\rho c$
κ_1	thermal conductivity, $cal\text{-}cm^{-1}\text{-}sec^{-1}\text{-}{}^\circ C^{-1}$
κ_2	parameter in expression for $f_{\bar{\bar{x}}_1}\left(\hat{\bar{x}}_1\right)$
λ	acoustic wavelength, cm

μ_1 viscosity of air, $g\text{-}cm^{-1}\text{-}sec^{-1}$

μ_2 parameter in expression for $f_{\hat{\bar{x}}_1}\left(\hat{\bar{x}}_1\right)$

ν parameter in expression for $f_{\hat{\bar{x}}_1}\left(\hat{\bar{x}}_1\right)$

ρ density of air, $g\text{-}cm^{-3}$

σ standard deviation of parameter indicated by subscript (for example, σ_{R_i} is standard deviation of R_i)

σ^2 variance of parameter indicated by subscript (for example, $\sigma_{R_i}^2$ is variance of R_i)

$\sigma_{x_i}^2$ variance of distance to ith pressure minimum, cm^2

χ acoustic reactance ratio, $X/\rho c$

$\Omega_{\hat{x}_1, \hat{\lambda}}$ correlation coefficient between best estimates of x_1 and λ

ω angular frequency, $rad\text{-}sec^{-1}$

Subscripts:

i   pressure minima positions counted from test specimen surface

m   mean value of random variable

0   value of quantity at test specimen surface or fixed value of radial coordinate

Abbreviations:

cgs   centimeter-gram-second system

dB   decibels referenced to 0.0002 $dynes/cm^2$ where 1 dyne = 0.00001 N

h.o.t.   higher order terms

I.D.   inside diameter

O.D.   outside diameter

SPL   sound pressure level, dB

Special notations:

erf( )   error function

˄   best estimates obtained from linear regression curve

˜   normalization by wavelength λ

SYSTEMATIC AND RANDOM ERRORS IN ACOUSTIC
IMPEDANCE MEASUREMENTS

The specific acoustic impedance at the surface of a homogeneous material is under-
stood to mean the ratio of the acoustic pressure to particle velocity suitably averaged
over a representative area of the material. Since the direct measurement of acoustic
particle velocity is not practical, acoustic impedance must be measured by indirect
means. The acoustic phenomenon central to the transmission line method of measuring
impedance is a one-dimensional standing-wave field. This standing-wave field is gen-
erated in a rigid wall tube by a source at one end and a sample of the test material at the
opposite end. For an inviscid acoustic medium, the resulting standing-wave field would
be characterized by equal pressure maxima and equal pressure minima located at half-
wavelength intervals along the normal to the material surface. The acoustic impedance
can be deduced from measurements of the ratio of the pressure maxima to the pressure
minima, the distance from the material surface to the first minimum, and the acoustic
wavelength.

Influences of the measurement apparatus and associated instrumentation on the
acoustic field and test specimen behavior cause systematic errors in the deduced imped-
ance. Also, there are random errors induced in the directly measured quantities due to
uncontrollable environmental and/or operational factors. The effect and control of sys-
tematic errors has been discussed in references 4, 5, and 6. This paper, therefore,
concentrates on the effect of random measurement errors on the deduced impedance;
however, systematic error sources relevant to this work are discussed briefly.

Systematic Errors

Systematic errors associated with the transmission line method for determining
impedance can be conveniently divided into the three following categories:

(a) Errors intrinsic to impedance tube operation

(b) Errors intrinsic to test specimen mounting

(c) Errors intrinsic to the measurement instrumentation

References 4 and 5 give detailed accounts of systematic errors intrinsic to the imped-
ance tube operation. Therefore, only the results relevant to this investigation are dis-
cussed here. A discussion of systematic errors intrinsic to the test specimen mounting
and measurement instrumentation is contained in the section entitled "Experimental
Setup and Test Procedure."

Effects of tube attenuation.- Figure 1 shows an impedance tube setup for deter-
mining the impedance across thin face-sheet materials. A variable cavity depth x_b
provides a known impedance for the wave A_2 transmitted through the test specimen.
The interaction of incident and reflected waves A_1 and B_1, respectively, produces a
standing-wave field. When measured by an axial pressure probe, a typical standing-
wave field appears as shown in the sketch of figure 1. In this sketch the coordinate sys-
tem origin is taken at the face of the test specimen with the positive axis running toward
the source. Successive standing-wave ratios $\left(\text{i.e., } p_{max}/p_{min}\right)$ and pressure minima
positions are denoted by S_i and x_i, respectively, where $i = 1, 2, \ldots, N$. Note that
S_0 denotes the ratio p_{max}/p_{min} at the specimen surface which is not directly
measurable.

Fluid viscosity and thermal conduction in the acoustic boundary layer near the tube
wall attenuate the wave motion (refs. 4 and 5). As figure 1 illustrates, this attenuation
creates an increase in the pressure minima (i.e., standing-wave ratios decrease) with
distance from the test specimen. Therefore, the standing-wave ratios S_i, which result
mainly from the test specimen-cavity system, are contaminated by tube-wall attenuation.
The resulting difference between the standing-wave ratios S_0 and S_1 is usually less
than 1 dB; however, the use of S_1 to approximate S_0 results in significant systematic
errors for some wavelengths and test specimen impedances.

The systematic error $S_0 - S_1$ can easily be corrected by conversion of the mea-
sured S_i to equivalent reflection coefficients R_i which approximate a straight line as
illustrated in the lower sketch of figure 2. A linear regression curve through the mea-
sured R_i then provides an estimate $\hat{R}_0$ of the reflection coefficient R_0. The formula
for converting the measured S_i to equivalent R_i, where S_i are measured in dB, is
given by

$$R_i = \frac{10^{S_i/20} - 1}{10^{S_i/20} + 1} \tag{1}$$

A secondary effect of tube-wall attenuation is a small shift of the pressure minima positions toward the specimen surface. In terms of acoustic wavelengths the expected shift in the first pressure minimum position according to reference 5 is

$$\Delta\left(\frac{x_1}{\lambda}\right) = \Delta\bar{x}_1 = \frac{1}{4\pi}\left(\frac{\alpha}{k}\right) \sinh\left[4\pi\left(\frac{\alpha}{k}\right)\bar{x}_1 + \ln\left(\frac{1}{R_1}\right)\right] \tag{2}$$

At 1.0 kHz, typical values of the parameters in equation (2) are

$$\frac{\alpha}{k} = 0.0017$$

$$\bar{x}_1 = 0.25 \text{ cm}$$

$$R_1 = 0.52 \qquad \left(S_1 = 10 \text{ dB}\right)$$

Therefore,

$$\Delta\bar{x}_1 = 0.0001 \text{ cm}$$

This result suggests that systematic shifts in pressure minima due to tube-wall attenuation are relatively insignificant except in those cases where R_1 becomes very small. In such cases, the pressure minima are not well defined because of the very small standing-wave ratios. Consequently, random errors would remain dominant.

Effect of backing cavity.- The impedance at the test specimen surface, as deduced from standing-wave measurements, is determined by the interaction of the impedance across the test specimen and the cavity impedance as illustrated in figure 1. For thin test specimens (i.e., thickness small relative to the wavelength) the total impedance at $x = 0$ is simply the sum of the specimen impedance and the cavity impedance. To avoid large systematic errors in the deduced impedance across the test specimen, the cavity depth must be adjusted for zero reactance. The cavity impedance is given by

$$Z_b = -\rho c \left(1 - j\frac{\alpha}{k}\right)^{-1} \cot kx_b \tag{3}$$

Therefore, the appropriate cavity depth is given by

$$x_b = \frac{c_0}{4f} \sqrt{\frac{T}{T_0}} \left(1 - \frac{\alpha}{k}\right) \tag{4}$$

where f is the driving frequency, T is the cavity gas temperature, α is the tube-wall absorption coefficient, k is the wave number, c_0 is a reference sound speed, and T_0 is the corresponding reference temperature.

Effect of finite probe size.- A systematic error in the measurement of pressure minima positions can arise because of the finite size of the axial pressure probe. From reciprocity considerations, the Rayleigh end correction of $0.85r_p$ for an unflanged pipe radiating into free space should be on the order of the probe end correction. However, the geometry of the probe end and of the surrounding hardware boundaries deviates significantly from the geometry for the Rayleigh end correction. Therefore, an experimental determination of the end correction is necessary. The experimental procedure for accomplishing this correction is discussed in the section entitled "Experimental Setup and Test Procedure."

Effect of structure-borne vibration.- Mechanical vibration of the impedance tube walls can cause serious systematic disturbances of the standing-wave field. In addition, the excitation of the pressure transducer by structure-borne vibrations can mask low sound pressure levels at pressure minima when the standing-wave ratios are large. Experimental design procedures to minimize these sources of systematic error are discussed further in the section entitled "Experimental Setup and Test Procedure."

Random Errors

The formulas for calculating the specific acoustic impedance at the surface of a test specimen from standing-wave data are well known (refs. 4, 5, and 6). These formulas, in slightly modified form for application in this work, are given for the resistance and reactance ratios, respectively, as

$$\theta = \frac{\left(\dfrac{1 - \hat{R}_0}{1 + \hat{R}_0}\right)\left(1 + \tan^2 2\pi\hat{x}_1\right)}{1 + \left(\dfrac{1 - \hat{R}_0}{1 + \hat{R}_0}\right)^2 \tan^2 2\pi\hat{x}_1} \tag{5a}$$

and

$$\chi = -\frac{\left[1 - \left(\dfrac{1 - \hat{R}_0}{1 + \hat{R}_0}\right)^2\right]\tan 2\pi\hat{\bar{x}}_1}{1 + \left(\dfrac{1 - \hat{R}_0}{1 + \hat{R}_0}\right)^2 \tan^2 2\pi\hat{\bar{x}}_1} \qquad (5b)$$

where $\hat{\bar{x}}_1 = \hat{x}_1/\hat{\lambda}$. The quantities $\hat{x}_1$ and $\hat{\lambda}$ are best estimates of the first pressure minimum position and the wavelength, respectively. The term $\hat{R}_0$ is a best estimate of the reflection coefficient at the specimen surface. The specific acoustic impedance ratio ζ at the test specimen surface is given by

$$\zeta = \frac{Z}{\rho c} = \frac{1}{\left(1 - j\dfrac{\alpha}{k}\right)}(\theta + j\chi) \qquad (6a)$$

where Z is the specific acoustic impedance at the specimen surface. Since $\dfrac{\alpha}{k} \ll 1$ for most measurement situations, it follows that

$$\zeta \approx \theta + j\chi \qquad (6b)$$

The effects of random measurement errors on $\hat{R}_0$ and $\hat{\bar{x}}_1$ and therefore on the impedance components θ and χ were analyzed by first calculating the variances σ_θ^2 and σ_χ^2 in terms of the variances $\sigma_{\hat{R}_0}^2$ and $\sigma_{\hat{\bar{x}}_1}^2$. The variances $\sigma_{\hat{R}_0}^2$ and $\sigma_{\hat{\bar{x}}_1}^2$ were then calculated from the estimated variances $\sigma_{R_i}^2$ and $\sigma_{x_i}^2$, respectively. The computations for σ_θ^2 and σ_χ^2 were accomplished using a standard technique from random process theory and a simplified approximate method, each of which is outlined.

Exact method.- The following assumptions were used to calculate σ_θ^2 and σ_χ^2 by the exact method:

(1) The probability density functions $f_{\hat{R}_0}(\hat{R}_0)$ and $f_{\hat{\bar{x}}_1}(\hat{\bar{x}}_1)$ are treated as statistically independent.

(2) The density functions $f_{R_i}(R_i)$ and $f_{x_i}(x_i)$ are normally distributed.

11

(3) If the respective means are suppressed, then

$$f_{R_i}(R_i) = f_{R_{i+1}}(R_{i+1})$$

$$f_{x_i}(x_i) = f_{x_{i+1}}(x_{i+1})$$

Therefore, from the random process theory given in reference 7

$$\sigma_\theta^2 = \int_{\hat{\bar{x}}_{1,m}-M\sigma_{\hat{\bar{x}}_1}}^{\hat{\bar{x}}_{1,m}+M\sigma_{\hat{\bar{x}}_1}} \int_{\hat{R}_{0,m}-M\sigma_{\hat{R}_0}}^{\hat{R}_{0,m}+M\sigma_{\hat{R}_0}} (\theta - \theta_m)^2 \, f_{\hat{R}_0}(\hat{R}_0) \, f_{\hat{\bar{x}}_1}(\hat{\bar{x}}_1) \, d\hat{R}_0 \, d\hat{\bar{x}}_1 \qquad (7a)$$

$$\sigma_\chi^2 = \int_{\hat{\bar{x}}_{1,m}-M\sigma_{\hat{\bar{x}}_1}}^{\hat{\bar{x}}_{1,m}+M\sigma_{\hat{\bar{x}}_1}} \int_{\hat{R}_{0,m}-M\sigma_{\hat{R}_0}}^{\hat{R}_{0,m}+M\sigma_{\hat{R}_0}} (\chi - \chi_m)^2 \, f_{\hat{R}_0}(\hat{R}_0) \, f_{\hat{\bar{x}}_1}(\hat{\bar{x}}_1) \, d\hat{R}_0 \, d\hat{\bar{x}}_1 \qquad (7b)$$

where the mean values θ_m and χ_m are given by

$$\theta_m = \int_{\hat{\bar{x}}_{1,m}-M\sigma_{\hat{\bar{x}}_1}}^{\hat{\bar{x}}_{1,m}+M\sigma_{\hat{\bar{x}}_1}} \int_{\hat{R}_{0,m}-M\sigma_{\hat{R}_0}}^{\hat{R}_{0,m}+M\sigma_{\hat{R}_0}} \theta f_{\hat{R}_0}(\hat{R}_0) \, f_{\hat{\bar{x}}_1}(\hat{\bar{x}}_1) \, d\hat{R}_0 \, d\hat{\bar{x}}_1 \qquad (8a)$$

$$\chi_m = \int_{\hat{\bar{x}}_{1,m}-M\sigma_{\hat{\bar{x}}_1}}^{\hat{\bar{x}}_{1,m}+M\sigma_{\hat{\bar{x}}_1}} \int_{\hat{R}_{0,m}-M\sigma_{\hat{R}_0}}^{\hat{R}_{0,m}+M\sigma_{\hat{R}_0}} \chi f_{\hat{R}_0}(\hat{R}_0) \, f_{\hat{\bar{x}}_1}(\hat{\bar{x}}_1) \, d\hat{R}_0 \, d\hat{\bar{x}}_1 \qquad (8b)$$

The integration limits in equations (7) and (8) were truncated symmetrically about the mean values $\hat{R}_{0,m}$ and $\hat{\bar{x}}_{1,m}$ at integer multiples of $\sigma_{\hat{R}_0}$ and $\sigma_{\hat{\bar{x}}_1}$, respectively, by trial and error. Values of $\sigma_{\hat{R}_0}$ and $\sigma_{\hat{\bar{x}}_1}$ were derived from estimates of $\sigma_{R_i}^2$ and $\sigma_{x_i}^2$.

The variances $\sigma_{R_i}^2$ and $\sigma_{x_i}^2$ were estimated by compiling statistical frequency distributions of the deviations of measured values of R_i and x_i from corresponding

12

best estimates obtained from their respective linear regression curves. A typical regression curve for four measured reflection coefficients (i.e., $N = 4$) is shown in the sketch of figure 2. The best estimate of the specimen reflection coefficient is the extrapolated value $\hat{R}_0$ obtained from the regression curve at $x = 0$. Likewise $\hat{R}_i$ are the best estimates of R_i taken from the regression curve at the corresponding x_i. The deviations $\left(R_i - \hat{R}_i\right)$ are shown in figure 3 as a probability density histogram. Superimposed on figure 3 is a normal probability density function adjusted so that the integrated areas are equal between the deviations -0.003 and 0.003. Therefore, an estimate of $f_{R_i}\left(R_i\right)$ is given by

$$f_{R_i}\left(R_i\right) = \frac{1}{\sigma_{R_i}\sqrt{2\pi}} \exp\left[-\frac{\left(R_i - R_{i,m}\right)^2}{2\sigma_{R_i}^2}\right]$$

(9)

where $\sigma_{R_i} \approx 0.001$.

An entirely similar procedure for estimating the density functions $f_{x_i}(x_i)$ is illustrated in figures 4 and 5. In this case the result is

$$f_{x_i}\left(x_i\right) = \frac{1}{\sigma_{x_i}\sqrt{2\pi}} \exp\left[-\frac{\left(x_i - x_{i,m}\right)^2}{2\sigma_{x_i}^2}\right]$$

(10)

where $\sigma_{x_i} \approx 0.0096$ cm.

To evaluate the integrals in equations (7) and (8), values of $\sigma_{\hat{R}_0}$ and $\sigma_{\hat{x}_1}$ are needed to define the integration limits and to construct $f_{\hat{R}_0}\left(\hat{R}_0\right)$ and $f_{\hat{x}_1}\left(\hat{x}_1\right)$ which appear in the integrands. The random variable $\hat{R}_0$ is linearly dependent on the measured random variables R_i through the linear regression curve shown in figure 2. Therefore, from the equation for the linear regression curve and the definition of variance, it follows that

$$\sigma_{\hat{R}_0}^2 = \sigma_{R_i}^2\left(\frac{A}{NA - B^2}\right)$$

(11)

13

where

$$A = \sum_{i=1}^{N} x_i^2$$

$$B = \sum_{i=1}^{N} x_i$$

and

$$N \geq 2$$

The integer N denotes the total number of x_i and corresponding R_i measured for a given wavelength.

The procedure for calculating $\sigma_{\bar{x}_1}^2$ from $\sigma_{x_i}^2$ is straightforward but lengthy. The procedure is outlined and the results are stated. The first step is to calculate $\sigma_{\bar{x}_i}^2$ and $\sigma_{\hat{\lambda}}^2$ in terms of $\sigma_{x_i}^2$. The same procedure used to obtain equation (11) gives

$$\sigma_{\bar{x}_i}^2 = \sigma_{x_i}^2 \left(\frac{A - 2B + N}{NA - B^2} \right) \tag{12a}$$

$$\sigma_{\hat{\lambda}}^2 = \sigma_{x_i}^2 \left(\frac{2N}{NA - B^2} \right) \tag{12b}$$

where

$$A = \sum_{i=1}^{N} n_i^2$$

$$B = \sum_{i=1}^{N} n_i$$

and

$$N \geq 2$$

14

The behavior of the ratios $\sigma_{\hat{\bar{x}}_1}^{\,2}/\sigma_{x_i}^{\,2}$ and $\sigma_{\hat{\lambda}}^{\,2}/\sigma_{x_i}^{\,2}$ is shown by the respective curves of figures 6 and 7. These curves show that both $\sigma_{\hat{\bar{x}}_1}^{\,2}$ and $\sigma_{\hat{\lambda}}^{\,2}$ decrease with increasing N; however, $\sigma_{\hat{\lambda}}^{\,2}$ decreases at a much greater rate than does $\sigma_{\hat{\bar{x}}_1}^{\,2}$.

Although the density functions $f_{x_i}(x_i)$ are assumed normal, the density function $f_{\hat{\bar{x}}_i}(\hat{\bar{x}}_i)$ will not be normal since the random variable transformation $\hat{\bar{x}}_1 = \hat{x}_1/\hat{\lambda}$ is non-linear. The technique for deriving $f_{\hat{\bar{x}}_1}(\hat{\bar{x}}_1)$ from $f_{\hat{x}_1}(\hat{x}_1)$ and $f_{\hat{\lambda}}(\hat{\lambda})$ is given in reference 7. The result is

$$f_{\hat{\bar{x}}_1}(\hat{\bar{x}}_1) = \frac{1}{2\sqrt{\pi}\,\sigma_{\hat{x}_1}\sigma_{\hat{\lambda}}\mu_2\sqrt{1 - \Omega_{\hat{x}_1,\hat{\lambda}}}}\left[\exp\left(\frac{\nu^2}{\mu_2^2} - \kappa_2\right)\right]\left[\exp\left(-\frac{\nu^2}{\mu_2}\right) + \frac{2\sqrt{\pi}}{\sqrt{\mu_2}}\,\mathrm{erf}\left(\frac{\nu\sqrt{2}}{\sqrt{\mu_2}}\right)\right] \tag{13a}$$

where

$$\nu = \frac{1}{2\left(1 - \Omega_{\hat{x}_1,\hat{\lambda}}^2\right)\sigma_{\hat{x}_1}\sigma_{\hat{\lambda}}}\left[\left(\Omega_{\hat{x}_1,\hat{\lambda}}\hat{\lambda}_m - \hat{x}_{1,m}\frac{\sigma_{\hat{\lambda}}}{\sigma_{\hat{x}_1}}\right)\hat{\bar{x}}_1 + \left(\Omega_{\hat{x}_1,\hat{\lambda}}\hat{x}_{1,m} - \hat{\lambda}_m\frac{\sigma_{\hat{x}_1}}{\sigma_{\hat{\lambda}}}\right)\right] \tag{13b}$$

$$\mu_2 = \frac{1}{2\left(1 - \Omega_{\hat{x}_1,\hat{\lambda}}^2\right)\sigma_{\hat{x}_1}^{\,2}}\left[\left(\hat{\bar{x}}_1 - \Omega_{\hat{x}_1,\hat{\lambda}}\frac{\sigma_{\hat{x}_1}}{\sigma_{\hat{\lambda}}}\right)^2 + \left(\frac{\sigma_{\hat{x}_1}}{\sigma_{\hat{\lambda}}}\right)^2\left(1 - \Omega_{\hat{x}_1,\hat{\lambda}}^2\right)\right] \tag{13c}$$

$$\kappa_2 = \frac{1}{2\left(1 - \Omega_{\hat{x}_1,\hat{\lambda}}^2\right)\sigma_{\hat{x}_1}^{\,2}}\left[\left(\hat{x}_{1,m} - \Omega_{\hat{x}_1,\hat{\lambda}}\hat{\lambda}_m\frac{\sigma_{\hat{x}_1}}{\sigma_{\hat{\lambda}}}\right)^2 + \hat{\lambda}_m^{\,2}\left(\frac{\sigma_{\hat{x}_1}}{\sigma_{\hat{\lambda}}}\right)^2\left(1 - \Omega_{\hat{x}_1,\hat{\lambda}}^2\right)\right] \tag{13d}$$

The quantities $\hat{x}_{1,m}$ and $\hat{\lambda}_m$ are the true mean values of the random variables $\hat{x}_1$ and $\hat{\lambda}$. In the data gathering process only one set of x_i values was obtained for each wavelength on a given test run. Therefore, $\hat{x}_{1,m}$ and $\hat{\lambda}_m$ were estimated

15

by $\hat{x}_1$ and $\hat{\lambda}$. An expression for the correlation coefficient $\Omega_{\hat{x}_1, \hat{\lambda}}$ is given by

$$\Omega_{\hat{x}_1, \hat{\lambda}} = \frac{N - B}{\sqrt{NA - B^2} \sqrt{AN - 2BN + N^2}} \tag{14}$$

The behavior of $\Omega_{\hat{x}_1, \hat{\lambda}}$ as a function of N is shown in figure 8. As would be expected, $\Omega_{\hat{x}_1, \hat{\lambda}}$ decreases with increasing N.

Equations (5) and (7) to (15) permit exact calculations of σ_θ^2 and σ_χ^2 from experimentally determined input parameters. A computer program was prepared to perform these calculations for several representative values of the various parameters. Because a large amount of central processing unit (CPU) time (typically, 100 sec) was required to perform a trend analysis, a simplified approximate analysis was developed. The results of the exact and approximate analysis are compared in this paper. However, before discussing these comparisons, the approximate analysis procedure is outlined.

Approximate analysis.- The approximate analysis follows the procedure given in reference 7 which makes use of the assumptions

(a) The density functions $f_{\hat{R}_0}\left(\hat{R}_0\right)$ and $f_{\hat{x}_1}\left(\hat{x}_1\right)$ are smooth and concentrated in the vicinity of $\hat{R}_{0,m}$ and $\hat{x}_{1,m}$.

(b) The impedance components $\theta\left(R_0, x_1\right)$ and $\chi\left(R_0, x_1\right)$ are smooth in the vicinity of $\hat{R}_{0,m}$ and $\hat{x}_{1,m}$ and do not take on large values out of the neighborhood of $\hat{R}_{0,m}$ and $\hat{x}_{1,m}$.

(c) The random variables $\hat{R}_0$ and $\hat{x}_1$ are uncorrelated.

The first terms of the Taylor series expansion of the resistance ratio about the mean values $R_{0,m}, x_{1,m}$ give

$$\theta\left(\hat{R}_0, \hat{x}_1\right) \approx \theta\left(\hat{R}_{0,m}, \hat{x}_{1,m}\right) + \left.\frac{\partial \theta}{\partial \hat{R}_0}\right]_{\hat{R}_{0,m}, \hat{x}_{1,m}}\left(\hat{R}_0 - \hat{R}_{0,m}\right) + \left.\frac{\partial \theta}{\partial \hat{x}_1}\right]_{\hat{R}_{0,m}, \hat{x}_{1,m}}\left(\hat{x}_1 - \hat{x}_{1,m}\right) + \text{h.o.t.}$$

Therefore,

16

$$\left[\theta\left(\hat{R}_0, \hat{\bar{x}}_1\right) - \theta\left(\hat{R}_{0,m}, \hat{\bar{x}}_{1,m}\right)\right]^2 \approx \left(\frac{\partial \theta}{\partial \hat{R}_0}\right)^2_{\hat{R}_{0,m}, \hat{\bar{x}}_{1,m}} \left(\hat{R}_0 - \hat{R}_{0,m}\right)^2$$

$$+ \left(\frac{\partial \theta}{\partial \hat{\bar{x}}_1}\right)^2_{\hat{R}_{0,m}, \hat{\bar{x}}_{1,m}} \left(\hat{\bar{x}}_1 - \hat{\bar{x}}_{1,m}\right)^2$$

$$+ \left(\frac{\partial \theta}{\partial \hat{R}_0}\right)_{\hat{R}_{0,m}, \hat{\bar{x}}_{1,m}} \left(\frac{\partial \theta}{\partial \hat{\bar{x}}_1}\right)_{\hat{R}_{0,m}, \hat{\bar{x}}_{1,m}} \left(\hat{R}_0 - \hat{R}_{0,m}\right)\left(\hat{\bar{x}}_1 - \hat{\bar{x}}_{1,m}\right)$$

(15)

Substituting equation (15) into the integral of equation (7) and using assumptions (a), (b), and (c) yield

$$\sigma_\theta^2 \approx \left(\frac{\partial \theta}{\partial \hat{R}_0}\right)^2 \sigma_{\hat{R}_0}^2 + \left(\frac{\partial \theta}{\partial \hat{\bar{x}}_1}\right)^2 \sigma_{\hat{\bar{x}}_1}^2$$

(16a)

In the same manner, for the reactance ratio

$$\sigma_\chi^2 \approx \left(\frac{\partial \chi}{\partial \hat{R}_0}\right)^2 \sigma_{\hat{R}_0}^2 + \left(\frac{\partial \chi}{\partial \hat{\bar{x}}_1}\right)^2 \sigma_{\hat{\bar{x}}_1}^2$$

(16b)

where the derivatives in equations (16) are evaluated at the appropriate mean values $\hat{R}_{0,m}$ and $\hat{\bar{x}}_{1,m}$. Equations (16) are general forms relating the variance of a dependent variable to the variances of any number of independent variables. Therefore, the variance $\sigma_{\hat{\bar{x}}_1}^2$ can be written

$$\sigma_{\hat{\bar{x}}_1}^2 \approx \left(\frac{\partial \hat{\bar{x}}_1}{\partial \hat{x}_1}\right)^2 \sigma_{\hat{x}_1}^2 + \left(\frac{\partial \hat{\bar{x}}_1}{\partial \hat{\lambda}}\right)^2 \sigma_{\hat{\lambda}}^2$$

(17)

It is convenient to change independent variables in equation (16) as follows:

$$\hat{r}_0 = \frac{1 - \hat{R}_0}{1 + \hat{R}_0}$$

(18a)

17

$$\widehat{kx}_1 = 2\pi\hat{\bar{x}}_1 \tag{18b}$$

Therefore,

$$\sigma_\theta^{\ 2} \approx \left(\frac{\partial\theta}{\partial\hat{r}_0}\right)^2 \sigma_{\hat{r}_0}^{\ 2} + \left(\frac{\partial\theta}{\partial\widehat{kx}_1}\right)^2 \sigma_{\widehat{kx}_1}^{\ 2} \tag{19a}$$

$$\sigma_\chi^{\ 2} \approx \left(\frac{\partial\chi}{\partial\hat{r}_0}\right)^2 \sigma_{\hat{r}_0}^{\ 2} + \left(\frac{\partial\chi}{\partial\widehat{kx}_1}\right)^2 \sigma_{\widehat{kx}_1}^{\ 2} \tag{19b}$$

where

$$\sigma_{\hat{r}_0}^{\ 2} \approx \left(\frac{\partial r_0}{\partial\hat{R}_0}\right)^2 \sigma_{\hat{R}_0}^{\ 2} = \frac{4}{\left(1 + \hat{R}_0\right)^4} \sigma_{\hat{R}_0}^{\ 2} \tag{20a}$$

$$\sigma_{\widehat{kx}_1}^{\ 2} \approx \left(\frac{2\pi}{\hat{\lambda}}\right)^2 \left(\sigma_{\hat{x}_1}^{\ 2} + \hat{\bar{x}}_1^{\ 2} \sigma_{\hat{\lambda}}^{\ 2}\right) \tag{20b}$$

If the derivatives in equations (19a) and (19b) are calculated using equations (5), the following matrix equation can be written:

$$\begin{bmatrix} \sigma_\theta^{\ 2} \\ \\ \sigma_\chi^{\ 2} \end{bmatrix} = \begin{bmatrix} F_2^{\ 2} & 4\hat{r}_0 F_1^{\ 2} \\ \\ 4\hat{r}_0 F_1^{\ 2} & F_2^{\ 2} \end{bmatrix} \begin{bmatrix} \sigma_{\hat{r}_0}^{\ 2} \\ \\ \left(1 - \hat{r}_0\right)^2 \sigma_{\widehat{kx}_1}^{\ 2} \end{bmatrix} \tag{21a}$$

where

$$F_1 = \frac{\sec^2\widehat{kx}_1 \tan\widehat{kx}_1}{\left(1 + r_0^{\ 2} \tan^2\widehat{kx}_1\right)^2} \tag{21b}$$

18

$$F_2 = \frac{\sec^2 \widehat{kx}_1 \left(1 - \hat{r}_0^2 \tan^2 \widehat{kx}_1\right)}{\left(1 + \hat{r}_0^2 \tan^2 \widehat{kx}_1\right)^2} \qquad (21c)$$

Equations (18) and (21) are sufficient to calculate σ_θ^2 and σ_χ^2 in terms of the experimentally determined parameters. The behavior of the error propagation functions F_1 and F_2, as R_0 and $\bar{x}_1$ range through values likely to be encountered in typical impedance measurements, should provide insight as to which regions in the measurement space may be critical in regard to random measurement errors. Figures 9 and 10 show plots of F_1 and F_2, respectively, as functions of $\bar{x}_1$ with r_0 as a parameter. Note that r_0 can be physically interpreted as the reciprocal of the standing-wave ratio at the specimen surface, and kx_1 has been written as $2\pi\bar{x}_1$ to emphasize the fact that the distance to the first pressure minimum is measured in wavelengths. The parameter r_0 extends from 0.2 to 0.5, a range which corresponds to a standing-wave ratio range from 6.0 to 14.0 dB or a normal incidence absorption coefficient range from 0.56 to 0.89. The standing-wave ratios in dB corresponding to the values of r_0 are also shown in figure 9. Since the functions F_1 and F_2 are periodic with a period of π radians, their complete behavior is described over the $\bar{x}_1$ interval 0.00 to 0.50. Also, since the squares of F_1 and F_2 enter equation (21a), the behavior of the variances σ_θ^2 and σ_χ^2 is symmetrical about $\bar{x}_1 = 0.25$. The plots of figures 9 and 10 clearly indicate that random measurement errors tend to play an increasingly important role as $\bar{x}_1$ approaches 0.25 and as the standing-wave ratio increases beyond about 6.0 dB. This result corresponds to what would be expected from physical considerations because the acoustic particle velocity tends toward 0 as the impedance at the specimen surface increases indefinitely.

Comparison of exact and approximate analysis.- It remains to be seen whether the approximate analysis yields sufficiently accurate values of σ_θ and σ_χ given the restrictive assumptions underlying the analysis. Because computation time required in the approximate analysis is almost a hundredfold less than the time required in the exact analysis, a comparison of the results of the two analyses for some typical input parameters is worthwhile. The results of this comparison are shown in the curves presented in figures 11 to 16. In these figures, the solid curves represent the results from the approximate analysis and the dashed curves represent results from the exact analysis. Each set (parts (a) and (b)) of curves in figures 11 to 14 present computed values of the fractional standard deviations in nondimensional resistance σ_θ/θ and in nondimensional reactance σ_χ/χ plotted against the reflection coefficient R_0 with the nondimensional distance to the first pressure minimum $\bar{x}_1$ as a parameter. Realistic assumed values for the standard deviations in the reflection coefficients, the pressure minima positions,

19

and the acoustic wavelengths were chosen for the computations. Preliminary measurements suggested that the standard deviations in the reflection coefficients could be taken as approximately 0.002 and the standard deviations in the pressure minima positions could be taken to be approximately 0.02 cm. The four sets of computations were made for wavelengths corresponding to frequencies of 500, 1000, 2000, and 3000 Hz.

Figures 11(a), 12(a), 13(a), and 14(a) show that for $\bar{x}_1 = 0.1$ (i.e., provided the pressure minimum position is not in the immediate neighborhood of the quarter-wave point) the fractional standard deviations in the resistance σ_θ/θ increase relatively slowly as R_0 increases up to a value of about 0.7. Beyond $R_0 = 0.7$, however, σ_θ/θ increases rapidly and can exceed 6 percent for values of R_0 greater than about 0.975, a value which corresponds to a normal absorption coefficient of about 5 percent. As the pressure minimum position approaches the neighborhood of $\bar{x}_1 = 0.25$, σ_θ/θ begins to increase at smaller values of R_0. Furthermore, the increase becomes more pronounced with increasing frequency as indicated by the curves for $\bar{x}_1 = 0.200, 0.225$, and 0.245 (note scale change in fig. 13(a)). For the values of σ_{x_i} and σ_{R_i} chosen, the exact calculations (dashed curves) agree well with the approximate calculations. The discrepancy that does exist could result from the assumption in the approximate calculation that the probability density function is concentrated at the mean values.

Figures 11(b), 12(b), 13(b), and 14(b) present the same parametric study of the fractional standard deviation of the reactance ratio as was done in figures 11(a), 12(a), 13(a), and 14(a) for the resistance ratio. These figures show that σ_χ/χ is far more sensitive to values of $\bar{x}_1$ than was σ_θ/θ. Also, the behavior of σ_χ/χ with increasing R_0 is in general more complicated than was the behavior of σ_θ/θ. Again, because of the periodicity in the trigonometric functions involved in F_1 and F_2, the curves for $\bar{x}_1 > 0.25$ repeat the behavior of those for $\bar{x}_1 < 0.25$ and, therefore, were not plotted. Although the exact and approximate calculations agree well for the cases presented, the discrepancy between the two methods of analysis is generally greater for σ_χ/χ than for σ_θ/θ.

In addition to the comparisons of the approximate and exact analysis presented in figures 11 to 14, a comparison of the two methods of analysis for increasing values of σ_{R_i} and σ_{x_i} also yields interesting results. Figures 15 and 16 illustrate the results of this comparison for a frequency of 3.0 kHz. Figures 15(a) and (b) show the behavior of the fractional standard deviations in resistance and in reactance ratios, respectively, as a function of the standard deviation in reflection coefficients with quantities held constant as denoted in the figure key. As in the previous comparisons, the approximate calculations are shown by the solid lines, and the exact calculations are shown by the dashed lines with $\bar{x}_1$ as a parameter. Clearly, the approximate calculation begins to

break down for values of σ_{R_i} exceeding approximately 0.006 for both the fractional standard deviation in the resistance and in the reactance ratio. Figures 16(a) and (b) show the behavior of the fractional standard deviations in resistance and in reactance ratios, respectively, as a function of the standard deviation in the pressure minima positions, with quantities held constant as denoted in the figure key and with $\bar{x}_1$ as a parameter. In this case, the approximate calculation begins to break down for values of σ_{x_1} exceeding approximately 0.045 cm.

Figures 11 to 16 are believed to contain fairly representative comparisons of the approximate and exact methods for calculating the standard deviations of the impedance components when given the standard deviations in the reflection factors and in the pressure minima positions. In summary, the following observations are noted:

(1) Fractional standard deviations in resistance ratios tend to increase with increasing reflection coefficient.

(2) Fractional standard deviations in reactance ratios tend to develop complicated dependencies on the reflection coefficient as the frequency increases and as the pressure minima positions approach the quarter-wavelength point.

(3) Assumption (a) in the approximate analysis procedure appears to break down for values of σ_{R_i} and σ_{x_i} exceeding about 0.006 and 0.045 cm, respectively.

(4) For values of σ_{R_i} and σ_{x_i} below 0.006 and 0.045 cm, respectively, there is generally good agreement between the approximate and exact procedures; however, the discrepancy does increase with frequency and as $\bar{x}_1$ approaches the quarter-wavelength point. Also, the discrepancy is greater between the exact and approximate methods for σ_x/λ than for σ_θ/θ.

These results indicate that for the transmission line method of impedance measurements, the simple approximate equations (20) and (21) are suitable for providing conservative estimates for the variances in the impedance components in terms of the variances of the measured quantities σ_{R_i} and σ_{x_i} provided they do not exceed 0.006 and 0.045 cm, respectively. For a given test specimen, $\sigma_{R_0}^2$ and $\sigma_{x_i}^2$ are dependent on the quality of the particular experimental test setup and instrumentation, variability of environmental parameters such as temperature and ambient acoustic noise, and mechanical vibration.

Methods for estimating $\sigma_{R_0}^2$, $\sigma_{x_1}^2$, and σ_λ^2 may vary from mere guesses to elaborate statistical procedures. In this investigation these estimates were obtained by means of a simple compilation of statistical data associated with the linear regression curves for obtaining the estimates $\hat{R}_0$, $\hat{x}_1$, and $\hat{\lambda}$ as described in the section entitled

"Systematic Errors." The next section describes the data collection and processing in more detail.

DATA COLLECTION AND PROCESSING PROCEDURE

The random measurement errors associated with reflection factors R_i and pressure minima positions x_i can be quantified by constructing parametric probability densities $f_{x_i}(x_i, R_{i,m}, \lambda_m)$ and $f_{R_i}(R_i, x_{i,m}, \lambda_m)$ for each of a series of test specimens selected to produce a range of reflection coefficients between 0 and 1.0. Such a procedure would require several hundred repetitive measurements for each specimen and for each test wavelength. For example, 5 different reflection factors and 5 different wavelengths would imply 25 probability density functions. Experience with standing-wave measurements suggests that the dependency between $f_{x_i}(x_i, R_{i,m}, \lambda_m)$ and $f_{R_i}(R_i, x_{i,m}, \lambda_m)$ is probably very weak except in extreme and, from a practical standpoint, uninteresting situations where the test specimen is highly absorptive $\left(\text{i.e., } R_i \to 0\right)$ or highly reflective $\left(\text{i.e., } R_i \to 1\right)$. For the highly absorptive case, the standing-wave ratios are small (typically less than 1 dB); therefore, the random errors in pressure minima positions are large because the pressure minima positions are not well defined. On the other hand, when the reflection factors are large, the pressure minima positions are well defined, but the standing-wave ratios are large and tend to be unstable (i.e., subject to environmental disturbances). In addition, the acoustic wavelength also affects the statistical dependency between the random variables x_i and R_i.

The inordinate number of measurements required to rigorously construct the probability densities $f_{x_i}(x_i, R_{i,m}, \lambda_m)$ and $f_{R_i}(R_i, x_{i,m}, \lambda_m)$ can be dramatically reduced with the help of the following assumptions:

(1) Random measurement errors in reflection factors and pressure minima positions can be treated as statistically independent if the test specimen is not too highly absorptive or reflective.

(2) Deviations of individual measurements from their respective parent population means can be estimated by the deviations from their respective best estimates as obtained from linear regression curves (figs. 2 and 4) for a given impedance measurement.

Assumption (1) a   c   s plausible for the range of standing-wave ratios and wavelengths typically encou...ered in impedance measurements of most interest. The statistical bias resulting from assumption (1) will tend to cause overestimates of $\sigma_{R_i}^2$ and

$\sigma_{x_i}^2$ whereas the statistical bias resulting from assumption (2) will tend to cause under-estimates of $\sigma_{R_i}^2$ and $\sigma_{x_i}^2$.

Data Collection

To generate the deviations $R_i - \hat{R}_i$ and $x_i - \hat{x}_i$, at least three standing-wave ratios S_i and corresponding pressure minima positions x_i were measured for each test frequency. For the three test specimens designated A, B, and C, the total number of deviations measured exceeded 3500. A set of deviation measurements for a given specimen was collected over a frequency range of 0.5 to 3.5 kHz at typically 0.1-kHz intervals. Standing-wave ratios could be read in dB to three significant figures (i.e., ± 00.1 dB) and pressure minima positions in cm to four significant figures (i.e., ± 00.01 cm). Approximately 4 hr were required for collecting a data set. During that time the ambient temperature varied by approximately 2° C. From three to five data sets were collected for each specimen. As much as 6 months elapsed between some data sets. Except for test specimen A, the test specimens were removed and reinstalled in the test fixture between test runs.

Data Processing

A computer program was written to process the standing-wave ratio and pressure minima data. The computer program involved the following calculation steps:

(1) Conversion of S_i to R_i

(2) Calculation of linear regression curve coefficients for R_i and x_i

(3) Calculation of the best estimates $\hat{R}_i$, $\hat{x}_i$, $\hat{\lambda}$, $\hat{x}_i$, and $\hat{R}_0$

(4) Tabulation of $x_i - \hat{x}_i$ and $R_i - \hat{R}_i$ into selected class intervals

(5) Calculation of θ and χ from $\hat{R}_0$ and $\hat{x}_1$

(6) Calculation of fractional standard deviations σ_θ/θ and σ_χ/χ from $\sigma_{R_i}^2$ and $\sigma_{x_i}^2$ using the approximate analysis results given by equations (18) and (21)

The estimates of $\sigma_{R_i}^2$ and $\sigma_{x_i}^2$ in step (6) undergo improvement as more data are collected and tabulated according to step (4). After sufficient data are collected, the estimates $\sigma_{R_i}^2$ and $\sigma_{x_i}^2$, as shown, respectively, in figures 3 and 5, change little provided that operational and environmental parameters are held constant.

23

EXPERIMENTAL SETUP AND TEST PROCEDURE

Two equally important objectives were considered when the experimental setup
and test procedure were designed. One objective was to expedite the accumulation of
standing-wave impedance data by reading standing-wave ratios and pressure minima
positions directly from the monitoring instrumentation rather than through the inter-
mediary of a chart recording of the standing-wave pressure pattern. The second objec-
tive was to increase the precision and accuracy of the data by incorporating a few simple
and inexpensive techniques into the measurement procedure. A complete description of
the experimental setup and test procedure is given in the following sections.

Apparatus and Instrumentation

Impedance tube.- A block diagram of the impedance tube apparatus and associated
instrumentation is shown in figure 17. The apparatus consists of a main cylindrical tube
section in which : test specimen is mounted at one end by means of a test fixtui e that
provides an airtight seal around the specimen periphery. A variable cavity backing
depth is provided by a solid movable piston in a cylindrical tube attached to the test fix-
ture as shown in the sketch. The movable piston, 6.75 cm long, was machined from
steel and was fitted with O-ring seals at each end to provide an airtight sliding contact
with the machined inside surface of the cavity backing tube. Both the cavity backing tube
and the main tube have an inside diameter of 5.72 cm and a wall thickness of 0.64 cm.
The cavity backing tube and main tube have respective lengths of 60.95 cm and 83.83 cm.
A sound source consisting of a 60-W electromagnetic driver was coupled to the main
tube through an offset exponential horn as depicted in figure 17. A flexible coupling
decoupled mechanical vibration of the driver from the tube walls. A further precaution
was taken to reduce mechanical vibration of the tube walls by wrapping two layers of
asphalt-based damping tape over the entire length of the tubes.

Test specimen fixture.- The test specimen fixture was built to allow mounting of
test specimens 6.22 cm in diameter and up to 1.27 cm thick. Specimens less than
1.27 cm thick were bonded to an aluminum ring of sufficient length and thickness to pro-
vide an axial clamping force around a peripheral strip of the specimen. An active diam-
eter (i.e., diameter of specimen exposed to incident sound) of 5.72 cm remained. The
outside surface of the aluminum mounting ring was coated with a thin layer of silicone
release agent before installation to further insure an airtight seal between the incident
and backing cavity side of the specimen.

Acoustic pressure transducers and associated hardware.- Acoustic pressure signals
could be monitored simultaneously at two of three locations by condenser microphones
as shown in figure 17. A microphone 0.64 cm in diameter (channel 1) was used to

measure the acoustic pressure level at the piston face. The velocity through the specimen could be calculated (thin specimens only) from this pressure level. A 1.27-cm microphone (channel 2) was coupled to a movable steel probe tube (O.D. = 0.33 cm; I.D. = 0.19 cm; Length = 122 cm) to obtain relative acoustic pressure level measurements at points on the axis of the main tube. Microphone 2 was also isolated mechanically from the probe tube and tube support hardware. Fixed positions of both the axial probe and piston microphone could be read to four significant figures (i.e., ±00.01 cm) with the use of a specially constructed vernier, which was rigidly attached to the probe tube. The axial probe could also be continuously traversed by means of a variable speed motorized gear box for recording standing-wave patterns with a graphic level recorder if desired. A third microphone 0.33 cm in diameter (channel 3) was mounted so that its axis coincided with a radius of the main tube. This microphone was positioned 0.69 cm from the incident side of the specimen; it could be traversed manually in the radial direction up to the tube axis. Also the separation distance between the radial microphone probe and the specimen surface could be changed by an amount equal to the specimen mounting ring length by reversing the specimen orientation. The geometry of this apparatus together with three channels of acoustic measurement capability permitted measurements of standing-wave ratios, standing-wave pressure minima positions, and acoustic pressure variations across the specimen face.

Instrumentation.- A block diagram of the electronic instrumentation used in this experiment is also shown in figure 17. To insure reproducible measurement conditions at the test specimen, the acoustic pressure level was maintained at a constant level at the cavity back by monitoring the output of microphone 1. The signals from both the piston microphone and the axial probe microphone were filtered using a dual-channel 10-Hz-bandwidth tracking filter whose center frequency was automatically set by the oscillator frequency used to drive the acoustic source. A spectrum analyzer was used to monitor the overall spectral content of the signal at the piston face in order to detect malfunctions of equipment and/or nonlinear behavior of the acoustic source or test specimen. Generally, the harmonic content of the acoustic velocity at the specimen surface was maintained at about 20 dB below the fundamental acoustic velocity. The tracking filter outputs were read out visually on a dual-channel log-voltmeter which enabled acoustic pressure levels to be read to at least three significant figures over the entire test range.

Test Specimens

A summary of the geometrical and physical properties of the three test specimens used in this investigation are given in table I. The specimens were selected to cover the range of acoustic impedance of most interest in aircraft duct liner applications. In addition, the fiber metal specimens B and C were selected to show the contaminating

effects, if any, of mechanical resonance on the intrinsic acoustic impedance of the specimen. Specimen A was chosen as a control specimen in which the effects of mechanical vibration would be minimal and whose acoustic impedance could be computed theoretically.

Specimen A.- Test specimen A was a honeycomb-like ceramic structure with a porosity of 59 percent (195 channels/cm^2) and a thickness of 1.27 cm. The average individual channel diameter was 0.062 cm. This specimen was characterized by a very high flexural stiffness and low bulk density. These mechanical properties insured that no mechanical resonance of the specimen would contaminate the acoustic impedance in the frequency range of interest. Also the acoustic impedance of this specimen could be predicted on the basis of the classical theory for sound propagation in a tube (ref. 8). The nominal flow resistance for this specimen was 2.52 cgs rayls $\left(1 \text{ rayl} = 1 \dfrac{\text{bar}}{\text{cm/s}} = 10 \text{ Ns/m}^3\right)$.

Specimen B.- Test specimen B consisted of fiber metal fabricated from fibers of AISI type 347 stainless steel in a random arrangement. The fibers were compressed to a thickness of 0.09 cm. The mechanical properties of the specimen were such that the first mechanical resonance occurred within the test frequency range. The nominal flow resistance for this specimen was 57 cgs rayls.

Specimen C.- Test specimen C was also fabricated from fibers of AISI type 347 stainless steel compressed to a thickness of 0.35 cm. The nominal dc flow resistance of this specimen was 420 cgs rayls. The flexural stiffness and density were such that two mechanical resonances occurred within the range of frequencies investigated.

Tube Checkout Procedure for Systematic Errors in Reflection

Coefficients and Pressure Minima Positions

In addition to tube-wall absorption effects, systematic errors in the reflection coefficient and pressure minima positions can result from

(a) Excitation of higher order acoustic modes in the impedance tube caused by tube axis curvature at the probe entrance (see fig. 17) or other tube irregularities

(b) Departure of the backing cavity piston from assumed perfect reflectivity due to possible air leaks, microphone installation, vibration, thermal boundary layer, etc.

(c) Flanking transmission of sound through axial probe walls, acoustic excitation of axial probe, or other mechanical disturbances

(d) Excessively high ambient noise floor of acoustic medium in the impedance tube

(e) Electrical noise floor of measuring equipment

Unlike tube-wall absorption effects, possible systematic errors due to the above sources must be evaluated experimentally. The overall effect of the factors just listed can be estimated by observing the wave field in the tube in the absence of a test specimen; the backing cavity piston should be placed at the test specimen location (see fig. 17). This procedure is accomplished by observing amplitude and phase variations in the radial direction and by measuring reflection coefficients and pressure minima positions.

Radial amplitude and phase variations.- The radial microphone probe was manually traversed across about 75 percent of the tube diameter at each test frequency. The relative amplitude and phase changes between the axial microphone probe 2 and radial microphone probe 3 were observed with the axial probe fixed. Over the 0.5- to 3.0-kHz frequency range, the relative amplitude and phase changes were undetectable. Over the 3.0- to 3.5-kHz frequency range, the relative amplitude and phase changes were approximately 0.2 dB and 2^O, respectively. Above 3.6 kHz the relative amplitude and phase changes were clearly indicative of the existence of nonplanar waves. The theoretical cuton frequency of the first axisymmetric higher order mode was approximately 3.6 kHz.

Reflection coefficient behavior with no test specimen.- An additional check for anomalous behavior of the wave field in the impedance tube apparatus as well as the establishment of the signal noise floor was accomplished by measuring the standing-wave ratios and corresponding pressure minima positions with no test specimen present and with the piston face coincident with the specimen reference plane. This procedure also established the magnitude of possible systematic errors associated with the pressure minima positions and reflection coefficients. Figure 18 shows best estimates of the reflection coefficients and the corresponding best estimates of the nondimensional first pressure minima positions for frequencies of 0.5 to 3.5 kHz (at intervals of 0.1 kHz) with the SPL at the piston face held constant at 120 dB. The formula of equation (1) was used to calculate the reflection coefficients from the measured standing-wave ratios. These coefficients are plotted in figure 18 along the right-hand ordinate. These data show no anomalous behavior in the tube over the indicated frequency range. Although the reflection coefficients vary with frequency, they do not drop below 0.9950, and they remain above 0.9980 for most frequencies. These fluctuations are associated with the large standing-wave ratios in the tube as indicated by the dashed horizontal lines. Note that an S_i of 60 dB implies an SPL of 60 dB at a pressure minimum if the level at the piston face is 120 dB. These low SPL regions occupy very thin cross sections of the tube. Hence, any of the items listed under (c), (d), or (e) in the discussion of tube checkout procedure can cause an increase in the signal noise floor with an accompanying apparent reduction in the standing-wave ratio. This conjecture was supported by the fact that fluctuations by as much as 20 dB occur for the higher values of S_i. These measurements indicate that the piston behavior approaches that of a perfect reflector over the frequency range 0.5 to 3.5 kHz.

Pressure minima behavior with no test specimen.- For a perfectly rigid reflector the first pressure minima for all wavelengths should cluster around $\bar{x}_1 = 0.25$ provided random measurement errors only are present. However, the mean trend of the first pressure minima in figure 18 suggest a constant systematic error which would result in a displacement of the pressure minima positions 0.09 cm too far from the test specimen surface. As discussed previously in the subsection entitled "Systematic Errors," this discrepancy can be caused by a combination of scale calibration error and finite probe size effects, both of which are frequency independent. The systematic error in pressure minima positions was removed by incorporating a correction into the computer program used for the computations discussed previously in the "Data Processing" subsection.

In summary, the data of figure 18 demonstrate that the movable piston arrangement with the flush mounted microphone approaches a perfectly rigid reflector in its acoustical behavior. However, corrections for systematic errors in measurements for the pressure minima positions were necessary.

Tube calibration for random errors in reflection coefficients and pressure minima positions.- Random measurement errors occurring in the reflection coefficients and pressure minima positions were treated as properties of the impedance tube apparatus and its operating environment. As previously indicated, such treatment is a plausible procedure for moderate test specimen impedances. Hence, statistical data relevant to the random measurement errors can be combined as different specimens are tested. When sufficient statistical data have been collected to construct probability distributions, these distributions can be considered properties of this particular experimental arrangement just as was the case with systematic errors.

At least three pressure minima positions and corresponding standing-wave ratios were measured at each test frequency. Data collection efficiency was improved by recording pressure minima positions and SPL readings directly on data sheets from which computer inputs in the form of punched cards could be prepared. This procedure eliminated the need for time-consuming chart recordings of the entire standing-wave pattern. Accuracy in measurement of pressure minimum position was improved by taking two scale readings symmetrically spaced on either side of a given pressure minimum. A pressure minimum position was then obtained by taking the average of these readings.

RESULTS AND DISCUSSION

Impedance Measurement Results

Figures 19 to 26 present the experimental and theoretical results of this investigation for the three test specimens designated A, B, and C. Resistance and reactance

ratios together with their calculated fractional standard deviations are presented for each of the three test specimens as a function of frequency. In addition, the effect of systematic changes in the pressure minima positions is shown in these figures. For most of the tests, the backing cavity depth was adjusted to one-quarter wavelength for each test frequency, and the SPL at the cavity back was held constant at either 90 or 114 dB. The results of one test are presented in which the cavity depth was held constant. These results illustrate the possible systematic errors that may arise due to cavity antiresonance. Finally, for specimens B and C, the effect of mechanical vibration of the test specimen on the intrinsic acoustic impedance of the specimen is illustrated.

Specimen A

Effect of systematic measurement errors.- The effects of systematic errors in pressure minima positions and reflection coefficients were investigated by perturbing the measured quantities. Perturbations of approximately 5 times the respective standard deviations as obtained from the data of figures 3 and 5 were used. The effect of a perturbation of ± 0.05 cm in x_1 $\left(\text{i.e., } 5\sigma_{x_i}\right)$ is shown in figures 19 and 20 by the short-dashed curves that diverge about the measured impedance data as the frequency increases. The ± 0.05-cm perturbation was applied to the test data represented by the circular symbols. A similar calculation to evaluate the systematic errors due to a ± 0.005 perturbation $\left(\text{i.e., } \pm 5\sigma_{R_i}\right)$ in the reflection coefficient indicated a relatively insignificant effect compared with systematic errors in x_1 and therefore were not plotted. These results illustrate that the distance to the first pressure minimum expressed in wavelengths $\left(\text{i.e., } \bar{x}_1\right)$ is critical in the measurement of impedance values produced by specimen A. At 3.5 kHz, for instance, the resistance and reactance ratios can be increased by approximately 10 and 6 percent, respectively, by a 1.5-percent increase in $\bar{x}_1$ $\left(\text{i.e., } 0.05\text{-cm increase in } x_1\right)$. Note, however, that the three sets of data shown in figures 19 and 20 do not show a systematic increase in the scatter with increasing frequency. Systematic error in the measurements does not appear to be a significant problem over the time span and test conditions for which these measurements were obtained.

Effect of random measurement errors.- The effect of random measurement errors in pressure minima positions x_i and reflection coefficients R_i as specified by $\sigma_{x_i} = 0.0096$ cm and $\sigma_{R_i} = 0.001$, respectively, are shown in figures 19 and 20 by the long-dashed curves. These curves represent the fractional standard deviations in the resistance and reactance ratios, respectively, as a function of frequency. The curves were calculated using the approximate method as given in equations (18) to (21). In all cases, two sets of mean values for resistance and reactance were used in equations (18) to (21), corresponding to the two short-dashed curves representing the effect of a

± 0.05-cm perturbation on x_1. This was done to reveal the effect of mean value changes in resistance and reactance ratios on their respective fractional standard deviations. For specimen A, figure 19 shows that no significant change in the resistance ratio fractional standard deviation σ_θ/θ occurs for the changes in the mean values of the resistance ratio θ associated with the short-dashed curves. Also, for the reactance ratio standard deviation σ_χ/χ the mean value changes corresponding to the short-dashed curves of figure 20 were found not to have a significant effect; therefore, only one curve was plotted for σ_χ/χ. Examination of the magnitudes and trends of σ_θ/θ and σ_χ/χ plotted against frequency in figures 19 and 20, respectively, indicates a generally increasing effect of random errors with increasing frequency. However, σ_θ/θ and σ_χ/χ do not exceed approximately 2 and 1.3 percent, respectively. Specifically, at 3.4 kHz, there is a 67-percent probability that the measured resistance ratio lies within approximately 0.278 ± 0.006 ρc units. The range of variation corresponds closely to the amount of scatter observed in the three measurements at this frequency. For the reactance ratio the worst scatter appears to occur at 3.3 kHz where σ_χ/χ is about 1.1 percent. Therefore, there is 67-percent probability that the reactance ratio lies within approximately 1.52 ± 0.02 ρc units. In this case, the observed data scatter is slightly greater than $2\sigma_\chi$. These observations suggest that the contribution of random errors in pressure minima positions and reflection factors to the resultant scatter in the deduced impedance components is adequately described by the approximate calculation procedure given by equations (18) and (21) if the limits of σ_{x_i} and σ_{R_i} discussed in figures 15 and 16 are not exceeded.

Comparison of predicted and measured impedance.- Of the three test specimens only the surface impedance of specimen A could be predicted from existing classical theory relating to sound propagation through small tubes (ref. 8). An elementary application of the results of reference 8, together with the following assumptions, provides a predictive model for the surface impedance of specimen A backed by a cavity with an impedance Z_b:

(1) The propagation constant Γ for the entire length of a channel is equal to that for an infinitely long channel of the same radius.

(2) All channels have uniform circular cross sections of equal radii.

(3) The solid structure containing the channels is perfectly rigid.

(4) The ratio of channel diameter to channel separation is sufficiently near unity to eliminate the effects of the classical Rayleigh end correction (ref. 9).

With these assumptions, the surface impedance of a high porosity structure with parallel channels is given by

$$Z = \frac{Z_c}{P}\left(\frac{PZ_b + \tanh \Gamma l}{1 + PZ_b \tanh \Gamma l}\right) \qquad (22)$$

where Z_b is the impedance of the backing cavity, Z_c is the characteristic impedance of a single channel in the specimen, P is the specimen porosity, Γ is the propagation constant for waves propagating through a channel, and l is the channel length. If the channel backing cavity depth is set equal to a quarter-wavelength, as was the case in the investigation, then $Z_b = 0$ and equation (22) reduces to

$$Z = \frac{Z_c}{P} \tanh \Gamma l \qquad (23)$$

The propagation constant is given in reference 8 as

$$\Gamma = \sqrt{\frac{J_0\left(j^{3/2} s\right)}{J_2\left(j^{3/2} s\right)}} \sqrt{\frac{\gamma}{n}} \qquad (24a)$$

where s is the shear wave number. The quantity n is a complex polytropic constant describing the thermodynamic process in the channel and is given by reference 8 as

$$n = \left[1 - \frac{\gamma - 1}{\gamma} \frac{J_2\left(j^{3/2} \beta s\right)}{J_0\left(j^{3/2} s\right)}\right] \qquad (24b)$$

where β is the square root of the Prandtl number. The characteristic impedance is given by

$$Z_c = \frac{j\rho c}{2\Gamma \int_0^1 \left[1 - \frac{J_0\left(j^{3/2} \eta s\right)}{J_0\left(j^{3/2} s\right)}\right] \eta \, d\eta} \qquad (24c)$$

The shear wave number s and the Prandtl number β^2 are nondimensional quantities and are given, respectively, by

$$s = r_c\sqrt{\frac{\rho\omega}{\mu_1}} \qquad\qquad (24d)$$

$$\beta = \sqrt{\frac{\mu_1 c_p}{\kappa_1}} \qquad\qquad (24e)$$

The geometrical properties of specimen A needed in equations (23) and (24) are given in table I. In addition, the appropriate physical properties of the air in the channels of specimen A were taken to be

$$T = 25^\circ \ C$$

$$\rho = 0.0018 \ g\text{-}cm^{-3}$$

$$\mu_1 = 0.000181 \ g\text{-}cm^{-1}\text{-}sec^{-1}$$

$$c = 34\ 645 \ cm/sec$$

$$\beta = 0.88$$

$$\gamma = 1.402$$

The continuous curves of figures 19 and 20 show the predicted values of resistance and reactance ratios, respectively. The theory accurately predicts the measured resistance ratio at the lower frequencies but overpredicts the measured values by as much as 24 percent at the higher frequencies. For the reactance ratio, the theory overpredicts the measured values by about 14 percent at the lower frequencies; the overprediction increases to about 24 percent at the higher frequencies. A sensitivity study of equation (23) indicated that the predicted resistance and reactance ratios were much more sensitive to changes in the channel geometry than to changes in the gas temperature. These results suggest that the assumptions regarding end effects and channel geometry may be inadmissible for structures similar to specimen A; however, derivation of a more realistic model was beyond the scope of this investigation.

Specimen B

Specimen B consisted of felted stainless-steel fibers compressed into a thin (relative to the acoustic wavelength) sheet. The physical properties of the test specimen are

given in table I. This material has been a contender for the resistive element in air-craft duct liner applications. This particular specimen was chosen for this investigation because the resistance was such that near optimum performance of the standing-wave method for measuring impedance could be expected (i.e., the standing-wave ratios ranged between 3 and 20 dB).

Test results (quarter-wavelength backing cavity depth).- Figures 21 and 22 show the measured resistance and reactance ratios, respectively, for five sets of impedance data for test specimen B. These data were collected over a time span of approximately 9 months. Also, the specimen was removed and reinstalled between tests. Following the same format used in figures 19 and 20 for specimen A, a ±0.05-cm perturbation of the pressure minima positions for a typical test run (the impedance data collected on April 19, 1976, in this case) are shown by the short-dashed curves. Also, the long-dashed curves represent the behavior of the fractional standard deviations according to the mean values taken from the short-dashed curves.

Except for the sharp decrease in the resistance and reactance ratios in the vicinity of 1.4 kHz, the measured impedance values for all five sets of data exhibit uniform scatter across the entire 0.5- to 3.5-kHz frequency range. The dramatic decrease of the resistance and reactance ratios in the vicinity of 1.4 kHz results from the fundamental mechanical resonance frequency of the test specimen. This result was confirmed by calculating the resonance frequency based on estimates of the mechanical stiffness and surface density of the test specimen. (It should be noted that a cavity backing depth of a quarter-wavelength gives rise to the maximum possible acoustic pressure across the specimen surface.) These data provide an opportunity to better understand the relative contributions of systematic and random measurement errors.

As illustrated by the resistance ratio data in figure 21, the small percentage change (0.3 to 1.1 percent) in the fractional standard deviation over the 0.5- to 3.5-kHz frequency range does not adequately account for the generally uniform scatter in the data (outside the resonance region). On the other hand, systematic errors (associated with pressure minima measurements) between the different sets of measurements should produce diverging resistance values with increasing frequency as illustrated by the short-dashed curves. (However, no significant divergence was found for the reactance ratio when the measured positions were perturbed by ±0.05 cm.) These observations suggest that neither systematic errors intrinsic to the impedance tube nor random measurement errors are significant contributors to the observed scatter. The remaining likely source of data scatter was systematic error associated with the test specimen mounting conditions. This possibility can be supported by observing the detailed behavior with frequency of individual tests, especially in the vicinity of the mechanical resonance. In particular, note that the resistance ratio changed from 1.18 at 1.45 kHz for the test conducted on

April 19, 1976, to 0.95 at 1.45 kHz for April 21, 1976, or a change of 19 percent over a 2-day time period. Similar changes can be observed at other frequencies in the neighborhood of the mechanical resonance. At frequencies removed from the region of resonance, the variation of the measured resistance ratio among the different tests is approximately a uniform 4 percent.

The changes in the measured impedance values shown in figures 21 and 22 appear to be random in a manner independent of frequency. These observations suggest that the mounting conditions (i.e., conditions at the clamped boundary of the specimen) are chiefly responsible for the observed differences between the repeated impedance measurements. It should be noted that the axial clamping force around the specimen boundary was uniformly applied by means of machine bolts (1/4 in. diam.; 28 threads/in.) on which torque was applied until the specimen test fixture flange was seated against the impedance tube flange. This procedure was designed to allow the same amount of specimen boundary compression for each test run. The torque on the bolts was not necessarily the same from test to test.

Fixed cavity backing depth.- The design of practical duct liners for noise reduction applications may involve several layers of resistive face-sheet material together with various cavity depths to provide desired broadband impedance behavior. It is important to verify experimentally the predicted impedance of such structures. Therefore, the limitations of the particular impedance measurement method used to verify theoretical predictions should be understood. The transmission line method appears to have a fundamental limitation which will be illustrated with the results of a simple test. Specimen B was provided with a fixed cavity depth corresponding to a quarter-wavelength at 1.0 kHz. The impedance of the cavity-specimen combination was then measured over the 0.5- to 3.5-kHz frequency range with the sound pressure level at the cavity back held constant at 90 dB.

Figures 23 and 24 show the results of the fixed cavity depth impedance measurements for specimen B. When the backing cavity is a pure reactance, the measured resistance should theoretically be that caused by the face sheet alone as was the case for the variable quarter-wavelength cavity. However, when the acoustic half-wavelength is equal to the cavity depth, the acoustic particle velocity tends toward 0 at the specimen face. Physical intuition would suggest that the impedance would become very large since the acoustic pressure is held constant. The result illustrated in figure 23 for the resistance ratio plotted against frequency indicates that the intuitively suspected large impedance is achieved by the resistance becoming very large. Note that the theoretical cavity reactance (solid curve in fig. 24) becomes indeterminant at 2.0 kHz. The measured reactance closely follows the cavity reactance at low frequencies and becomes slightly greater than the cavity reactance with increasing frequency except in the vicinity of 2.0 kHz. This general deviation of the measured reactance toward more positive values

34

is due to the contribution of the positive reactance of specimen B to the cavity reactance. Since the measured reactance should theoretically never be less than the cavity reactance, the measured reactance at frequencies 1.9 kHz and 2.0 kHz in figure 24 must be regarded as anomalous. The possible effects of random measurement errors are indicated by the dashed curves in figures 23 and 24. Note that the fractional standard deviation rises dramatically near 2.0 kHz. At the frequency of 2.0 kHz where the maximum possible effect of random measurement errors occurs, the $2\sigma_\chi$ and $2\sigma_\theta$ ranges have been indicated on the measured impedance components in the figures. Although there is significant uncertainty in the impedance components due to random measurement error, the measured systematic increases in resistance are not fully explained by this uncertainty.

The results of the fixed cavity depth impedance measurements depicted in figures 23 and 24 suggest that the method does not produce valid results in the vicinity of those frequencies that produce multiple half-wavelengths in the backing cavity. The anomalous behavior of the measured impedance may be due to some as yet undetermined systematic error in the experimental setup.

Specimen C

Specimen C consisted of felted stainless steel fibers compressed into a thin (relative to the acoustic wavelength) sheet. The physical properties of the specimen are given in table I. Specimen C was chosen for this investigation because of its relatively high flow resistance of 420 cgs rayls. A flow resistance of 420 cgs rayls is as high as is likely to be encountered in any practical duct liner application. A material with such high resistance produces pressure minima positions in the vicinity of the critical quarter-wavelength point relative to the specimen face. These positions should reveal the relative importance of random and systematic errors for highly resistive specimens in view of the behavior of the error functions F_1 and F_2 (see figs. 9 and 10). Therefore, specimen C should serve to define the importance of random and systematic errors in the measured impedance for highly resistive specimens.

Figures 25 and 26 show the measured resistance and reactance ratios, respectively, for five sets of data collected over a time span of approximately 1 month. All the data were collected with a variable cavity backing depth of a quarter-wavelength. The specimen was removed and reinserted between tests. Following the same format used for specimens A and B, the effects of systematic errors of ±0.05 cm in the data for pressure minima positions collected on March 8, 1976, is shown by the short-dashed curves. The long-dashed curves represent the behavior of the fractional standard deviations using the mean values taken from the short-dashed curves.

A number of interesting features are evident from figures 25 and 26. First, two mechanical resonances contaminate the intrinsic acoustic impedance of the test specimen.

These resonances occur at approximately 0.67 and 2.15 kHz and correspond to the fundamental and first harmonic of the specimen acting as a clamped plate. Calculated resonance frequencies based on estimates of the specimen stiffness and area density indicated that the second resonance frequency corresponded to a vibrational mode with one circumferential node line. Second, in contrast to the situation for specimens A and B, the fractional standard deviations were significantly sensitive to the mean values of the impedance ratios taken from the short-dashed curves. For the case of the reactance, the 0.05-cm perturbation shifts the reactance to the vicinity of 0 over the frequency ranges from 1.0 to 2.0 kHz and from 2.5 to 3.4 kHz. The resulting effect on the reactance fractional standard deviation is meaningless. The corresponding long-dashed curve indicates that the fractional standard deviation exceeds 120 percent in these regions. The reactance data appear to support these analytical results since the reactance ratios exhibit more scatter with increasing frequency than do the resistance ratios. Third, the reactance ratios are critically sensitive to systematic error in the locations of pressure minima positions at the higher frequencies (see the short-dashed curves). In particular, careful examination of data for pressure minima positions for March 2, 1976, reveals that $\bar{x}_1$ experienced a 0.0023 increase (0.082 cm) between 2.7 and 2.8 kHz. This shift caused the sudden increase in the reactance ratio measured on that date. This sudden increase deviated from the pressure minima position trends for the other tests in which the pressure minima positions were moving toward the test specimen surface. A similar, apparently inconsistent, variation in pressure minimum position caused the sudden drop in the reactance ratio at 1.8 kHz for the data taken on March 3, 1976. Furthermore, corresponding disturbances in the resistance ratio trends are less severe. A careful review of the tube performance data did not reveal any significant inconsistencies. Therefore, these anomalies in the impedance must have resulted either from small disturbances in the probe position calibration or from contaminating influences of the specimen's mechanical impedance on the specimen's intrinsic acoustic impedance.

CONCLUSIONS

An investigation by the transmission line method of the effect of random and systematic errors associated with the measurement of normal incidence acoustic impedance in a zero-mean-flow environment indicated the following conclusions:

1. The effect of random measurement errors on impedance as measured by the transmission line method can be conveniently evaluated from estimates of the variances $\sigma_{x_1}^2$ and $\sigma_{R_0}^2$ where x_1 is the distance to the first pressure minimum and R_0 is the test specimen reflection coefficient.

2. Comparison of an exact and an approximate calculation procedure for obtaining the variances of the resistance and reactance ratios σ_θ^2 and σ_χ^2 indicated that computation times could be reduced by a factor of 100 without significant reduction in accuracy provided that standard deviations σ_{x_i} and σ_{R_i} do not exceed 0.045 cm and 0.006, respectively. The approximate formulas are given.

3. Random measurement errors in pressure minima positions and reflection coefficients for the experimental setup used in this investigation were found to approximate a normal probability distribution with standard deviations of 0.0096 cm and 0.001, respectively.

4. Calculated fractional standard deviations in the measured impedance components were generally found to increase with frequency; however, sensitivity to mean values of the measured quantities was found to vary markedly.

5. Conclusions 3 and 4 led to the belief that the uniform scatter in the impedance components observed to occur with increasing frequency for repeated measurements resulted from variations in test specimen mounting conditions.

6. Impedance measurements are, in general, more sensitive to random or systematic errors in the pressure minimum position than to random or systematic errors in the reflection coefficients.

7. Reliable resistance measurements can be obtained with constant cavity depth testing except in the vicinity of frequencies that produce multiples of a half-wavelength in the cavity.

These conclusions suggest that the transmission line method for measuring acoustic impedance is attractive for its theoretical and operational simplicity. Furthermore, the method allows the effects of random measurement errors (precision) to be quantified with ease. For the range of impedance values of interest in aircraft duct liner applications, pressure minimum position and standing-wave ratio measurements can easily be refined to limit impedance data scatter intrinsic to the tube to insignificant amounts (standard deviations not greater than 2 percent of the mean below 3.5 kHz). Careful consideration of the impedance measurements and error propagation analysis indicate that mechanical boundary conditions imposed on the specimen constitute the major source of inaccuracy in the measurement of isolated face-sheet impedance values. These boundary conditions

not only cause severe contamination of the intrinsic acoustic impedance of the test specimen in the neighborhood of mechanical resonances but may also cause most of the variation of the impedance components between identical tests.

Langley Research Center
National Aeronautics and Space Administration
Hampton, VA 23665
September 30, 1977

REFERENCES

1. Yaniv, Simone L.: Impedance Tube Measurement of Propagation Constant and Characteristic Impedance of Porous Acoustical Material. J. Acoust. Soc. America, vol. 54, no. 5, Nov. 1973, pp. 1138-1142.

2. Motsinger, R. E.; Kraft, R. E.; Zwick, J. W.; Vukelick, S. I.; Minner, G. L.; and Baumeister, K. J.: Optimization of Suppression for Two-Element Treatment Liners for Turbomachinery Exhaust Ducts. NASA CR-134997, 1976.

3. Plumblee, Harry E., Jr.; Dean, Peter D.; Wynne, George A.; and Burrin, Robert H.: Sound Propagation in and Radiation From Acoustically Lined Flow Ducts: A Comparison of Experiment and Theory. NASA CR-2306, 1973.

4. Beranek, Leo L.: Acoustic Measurements. John Wiley & Sons, Inc., 1949.

5. Lippert, W. K. R.: The Practical Representation of Standing Waves in an Acoustic Impedance Tube. Acustica, vol. 3, no. 3, 1953, pp. 15 160.

6. Impedance and Absorption of Acoustical Materials by the Tube Method. ASTM Designation: C384 - 58 (Reapproved 1972). Part 18 of 1975 Annual Book of ASTM Standards, c.1975, pp. 115-126.

7. Papoulis, Athanasios: Probability, Random Variables, and Stochastic Processes. McGraw-Hill Book Co., Inc., c.1965.

8. Tijdeman, H.: On the Propagation of Sound Waves in Cylindrical Tubes. J. Sound & Vib., vol. 39, no. 1, Mar. 1975, pp. 1-33.

9. Kinsler, Lawrence E.; and Frey, Austin R.: Fundamentals of Acoustics. Second ed. John Wiley & Sons, Inc., c.1962.

TABLE I.- GEOMETRICAL AND PHYSICAL PROPERTIES OF TEST SPECIMENS

Specimen designation	Description	Thickness, cm	Active diameter, cm	Bulk density, g/cm^3	Porosity, percent	Fiber diameter, cm	Channel diameter, cm	Flow resistance, cgs rayls (at 1 cm/sec)
A	Ceramic honeycomb	1.27	5.71	0.62	59.0	-----	0.062	2.52
B	Fiber metal	0.09	5.71	5.40	29.9	0.0112	----	57.0
C	Fiber metal	0.35	5.71	1.81	76.5	0.0004	----	420.0

39.
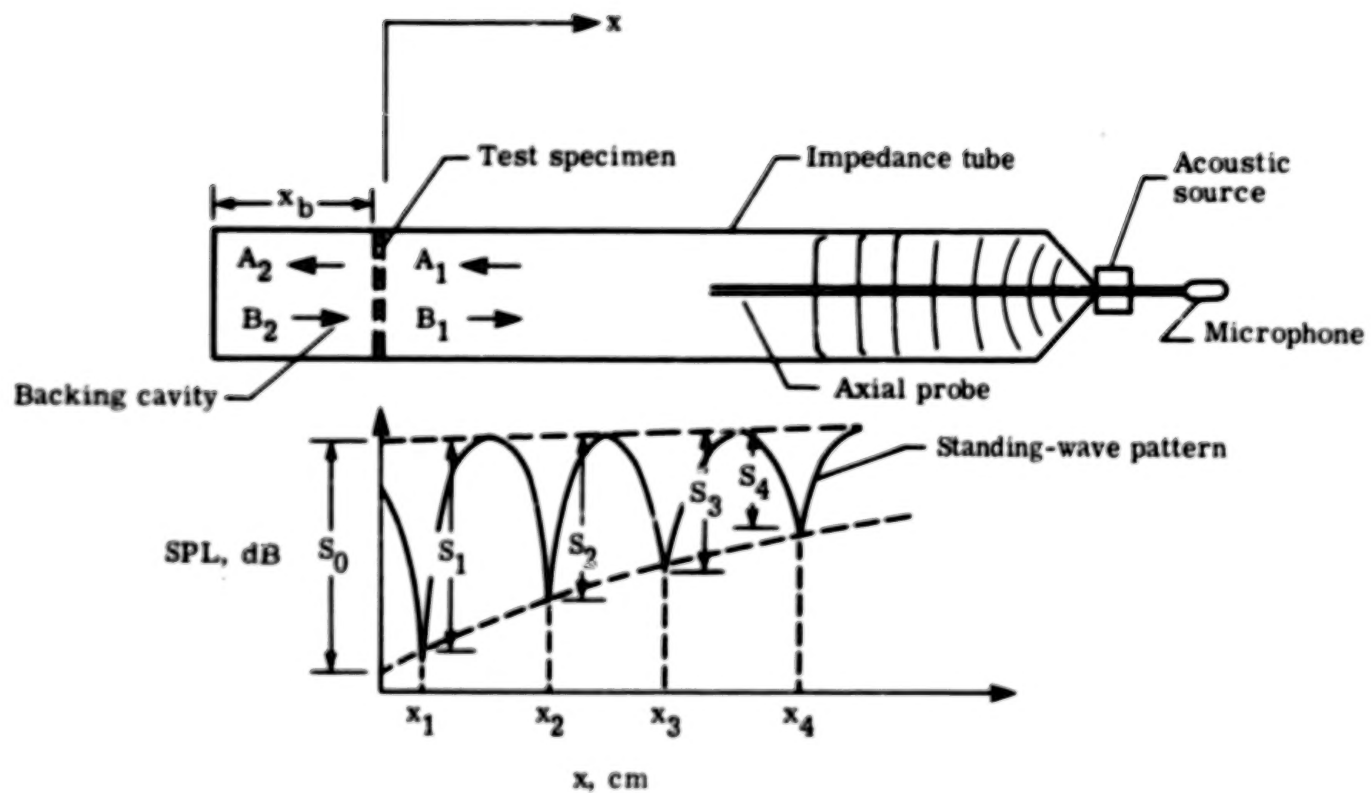
Figure 1.- Impedance tube and typical standing-wave pattern.

40.
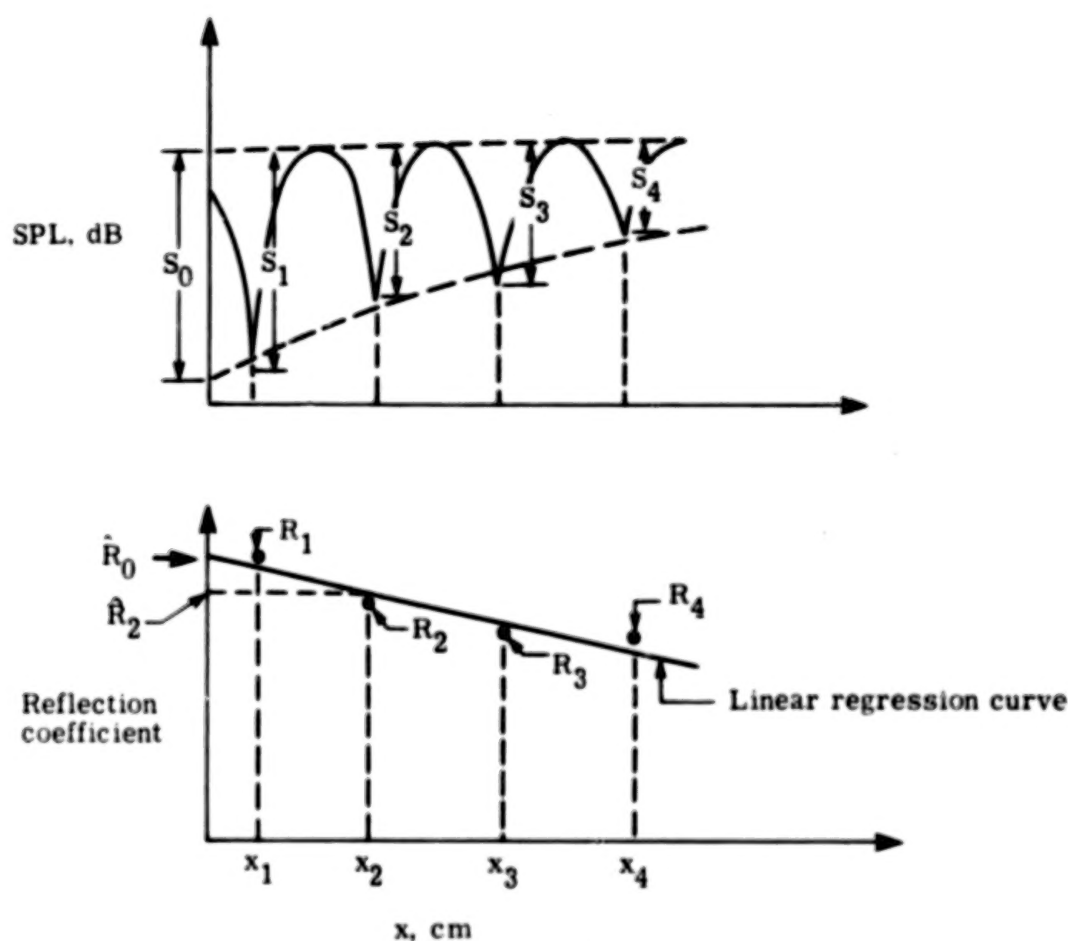
Figure 2.- Sketch showing correspondence between standing-wave ratios S_i and reflection coefficients R_i with linear regression curve to obtain $\hat{R}_0$.

41
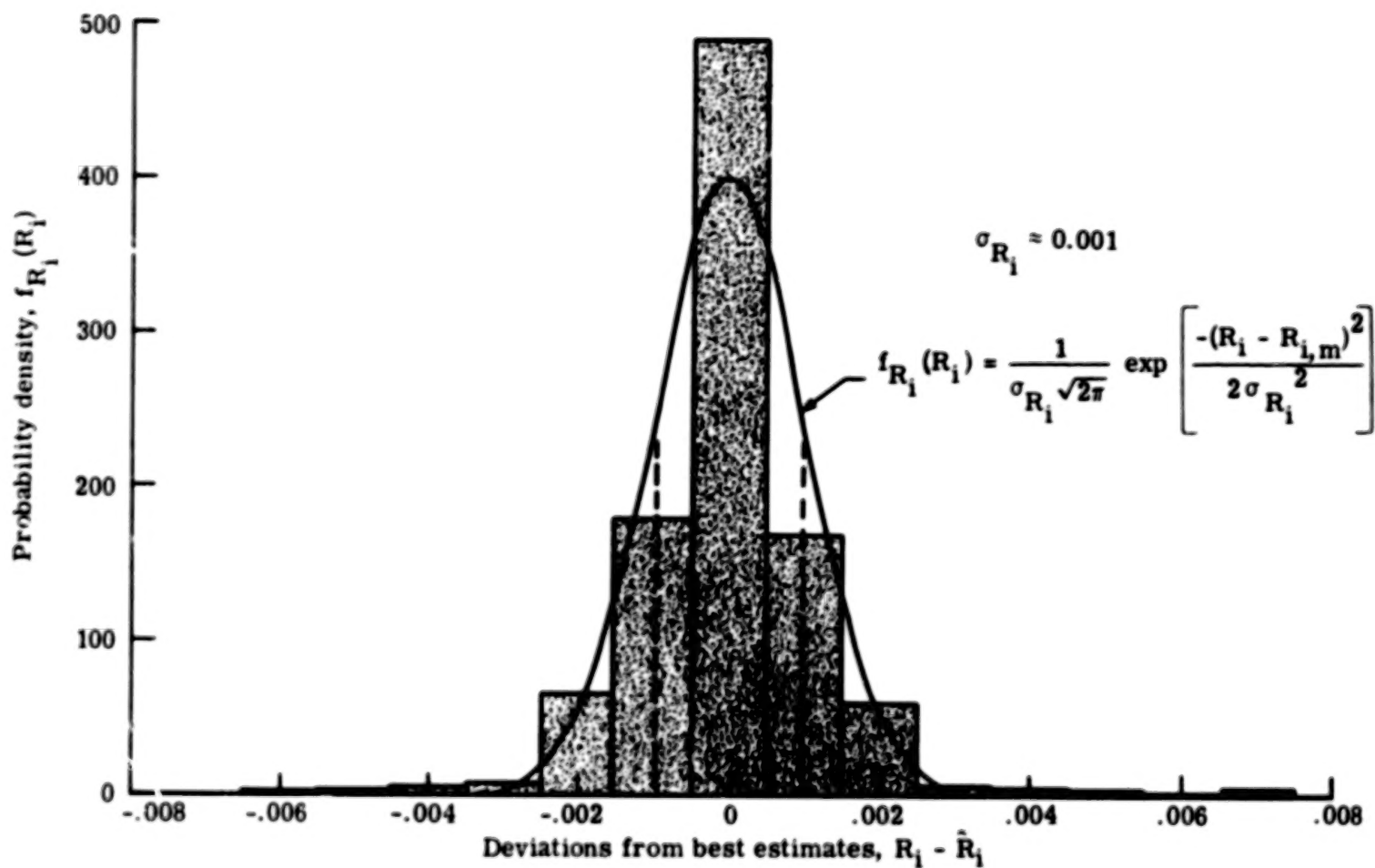
Figure 3.- Comparison of measured probability density histogram of reflection coefficient deviations from best estimates with normal probability law.

42.
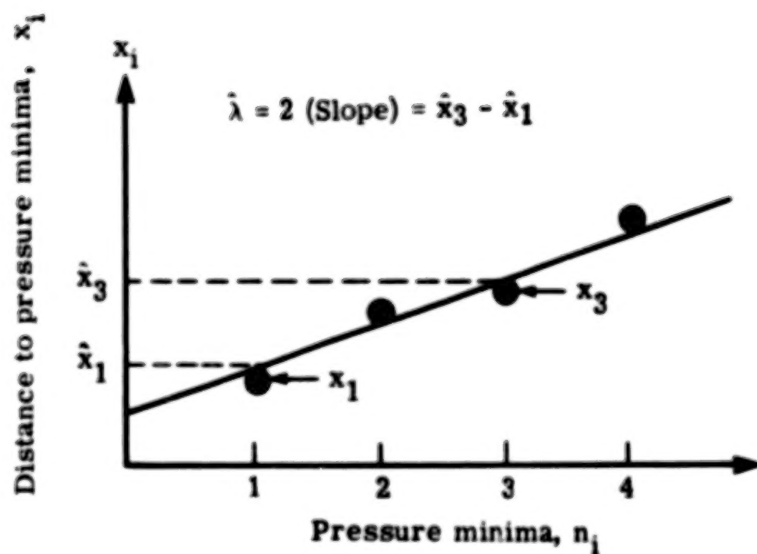
Figure 4.- Linear regression curve for obtaining best estimates of distance to first pressure minima and wavelength.

43.
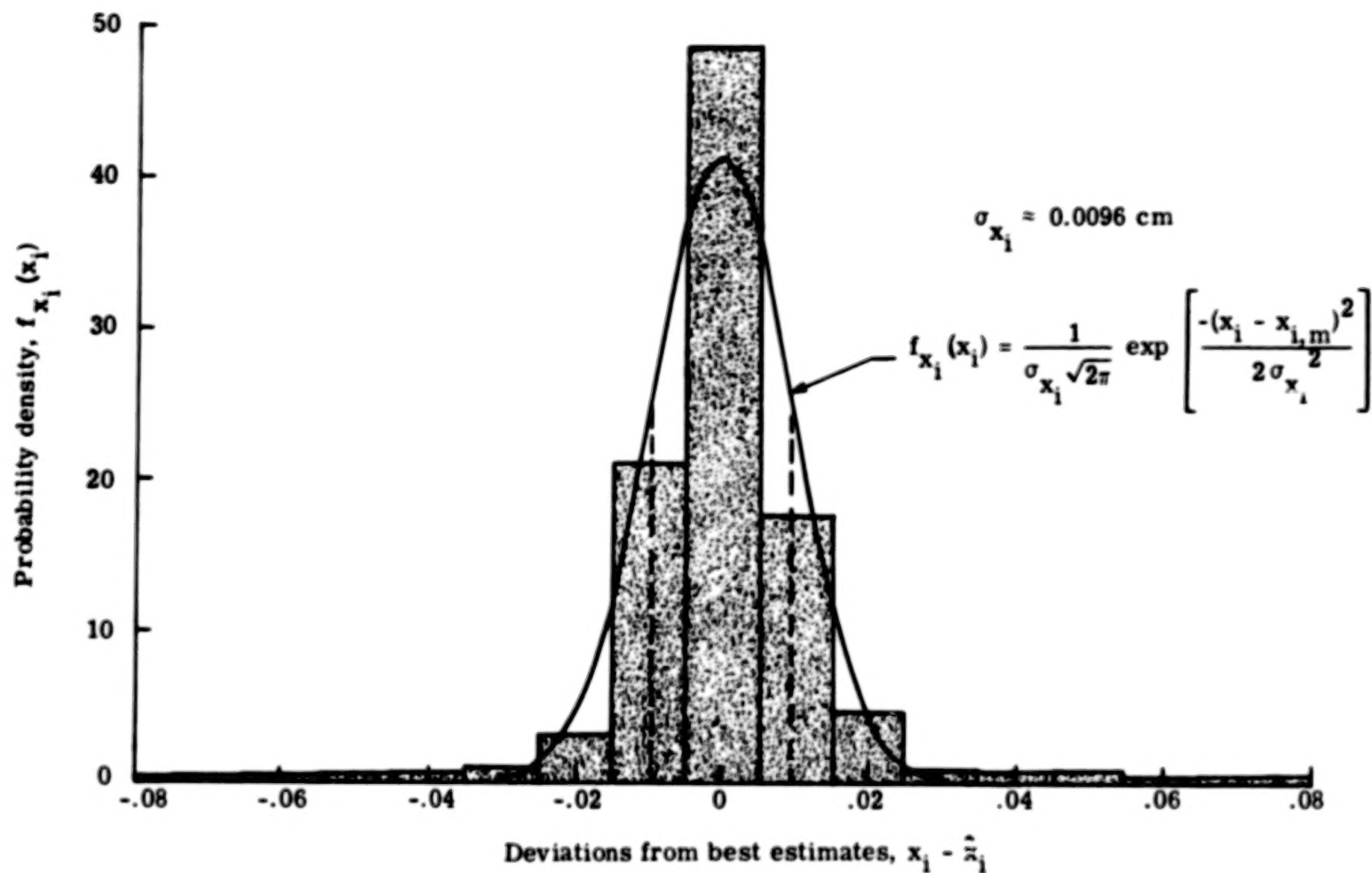
Figure 5.- Comparison of measured probability density histogram of pressure minima position deviations from best estimates with normal probability density.

44.
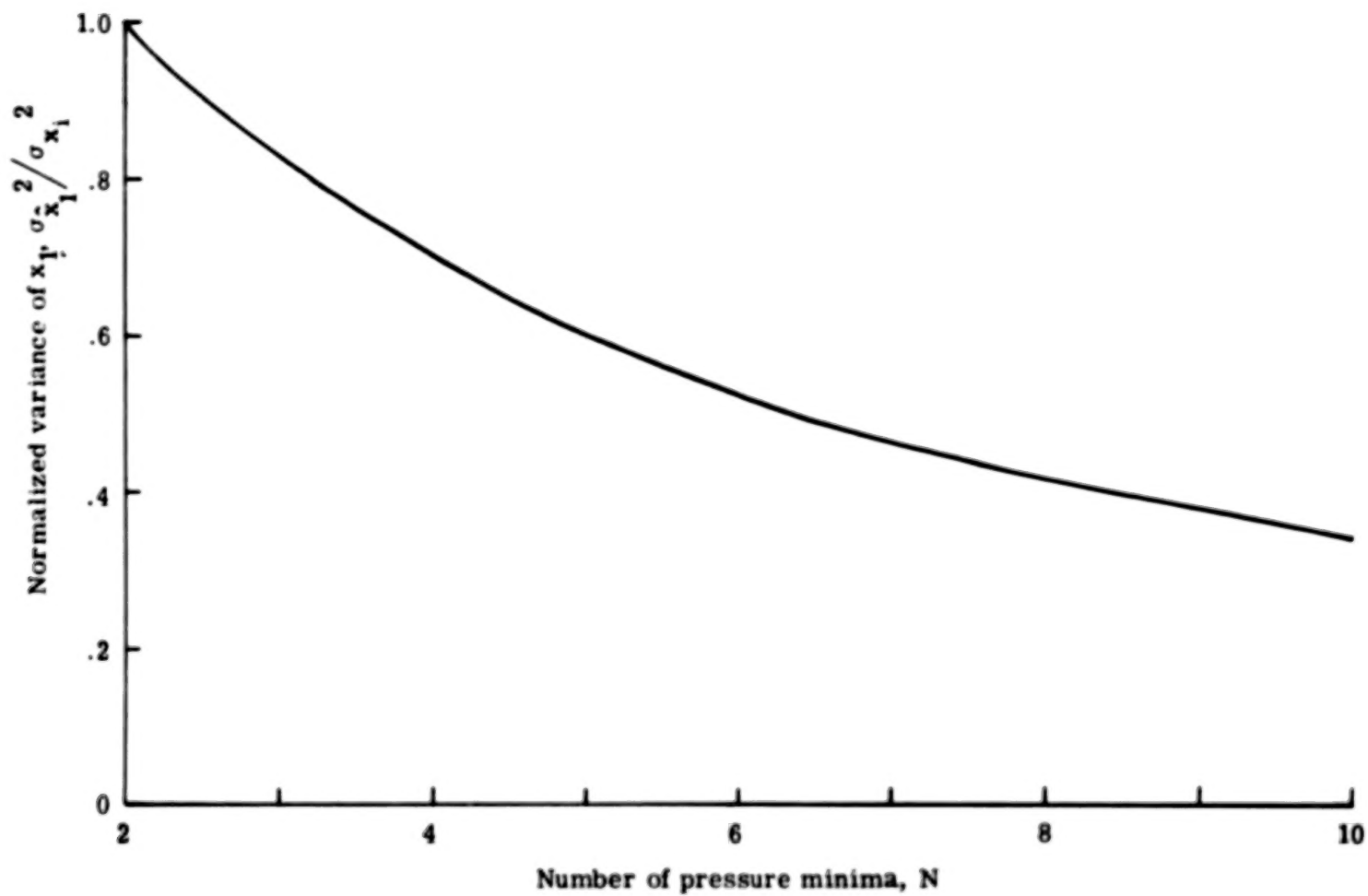
Figure 6.- Normalized variance of $\hat{x}_1$ plotted against number of measured pressure minima.

45.
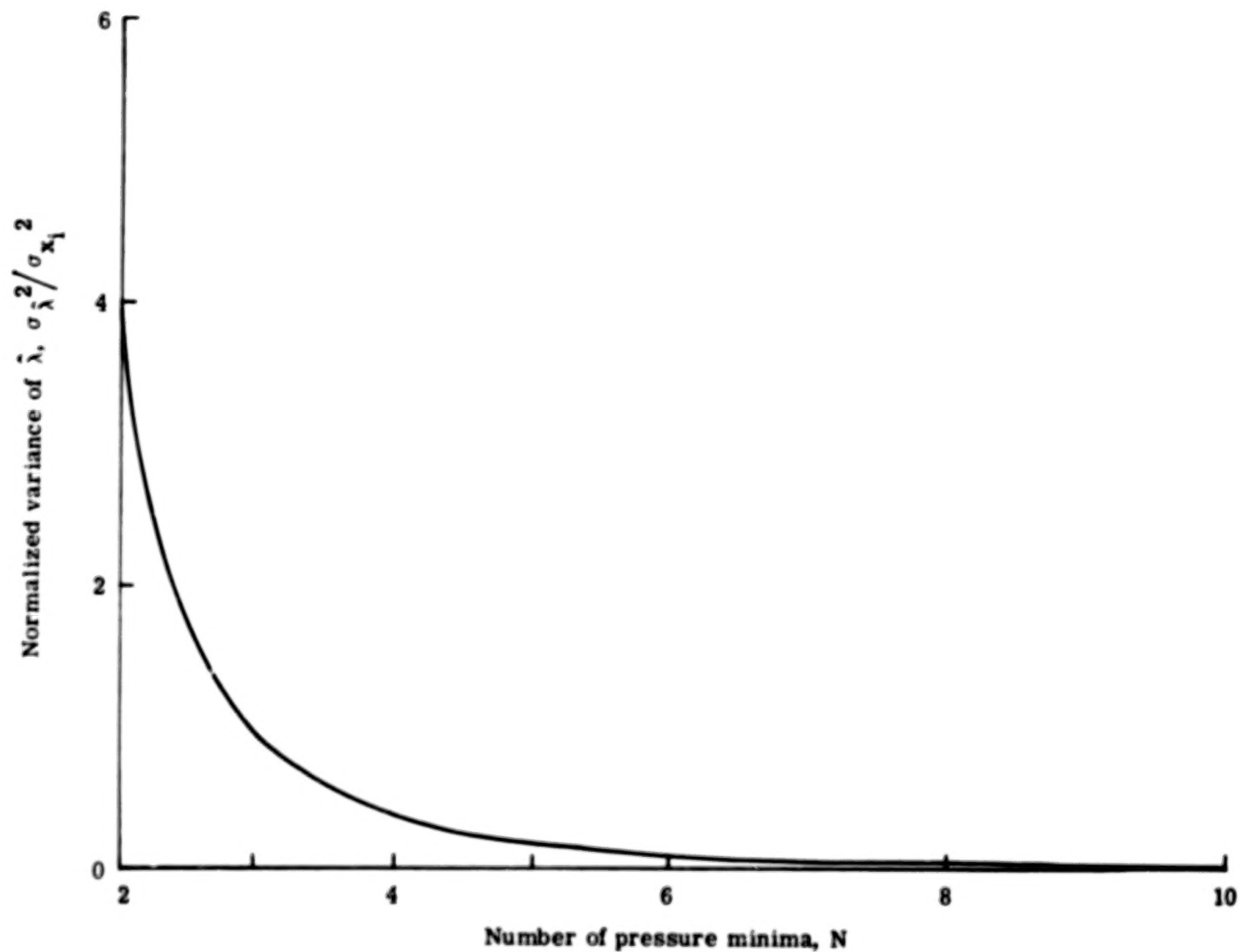
Figure 7.- Normalized variance of $\hat{\lambda}$ plotted against number of measured pressure minima.
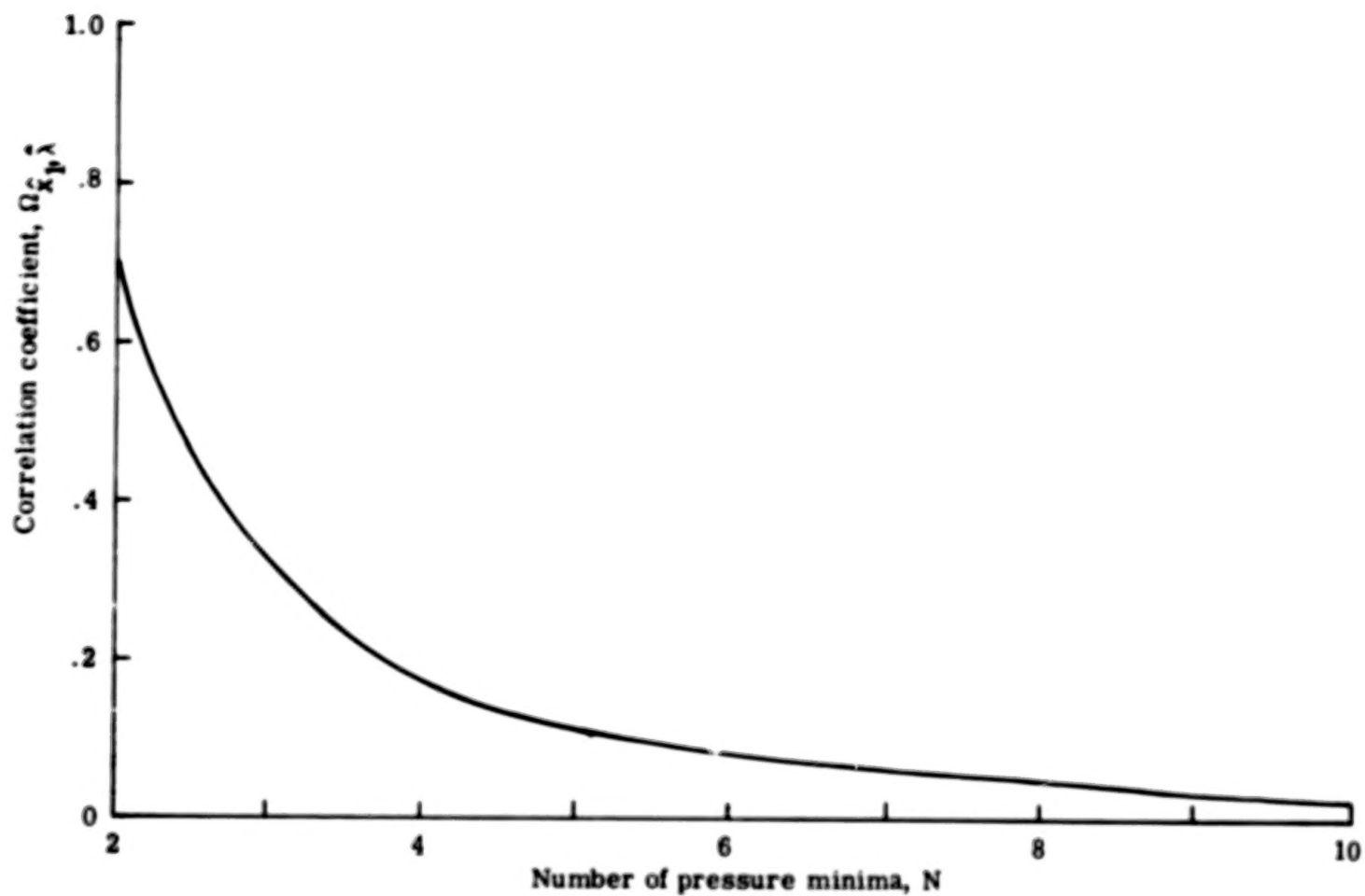
Figure 8.- Correlation coefficient $\Omega_{\hat{x}_1, \hat{\lambda}}$ plotted against number of measured pressure minima.

47
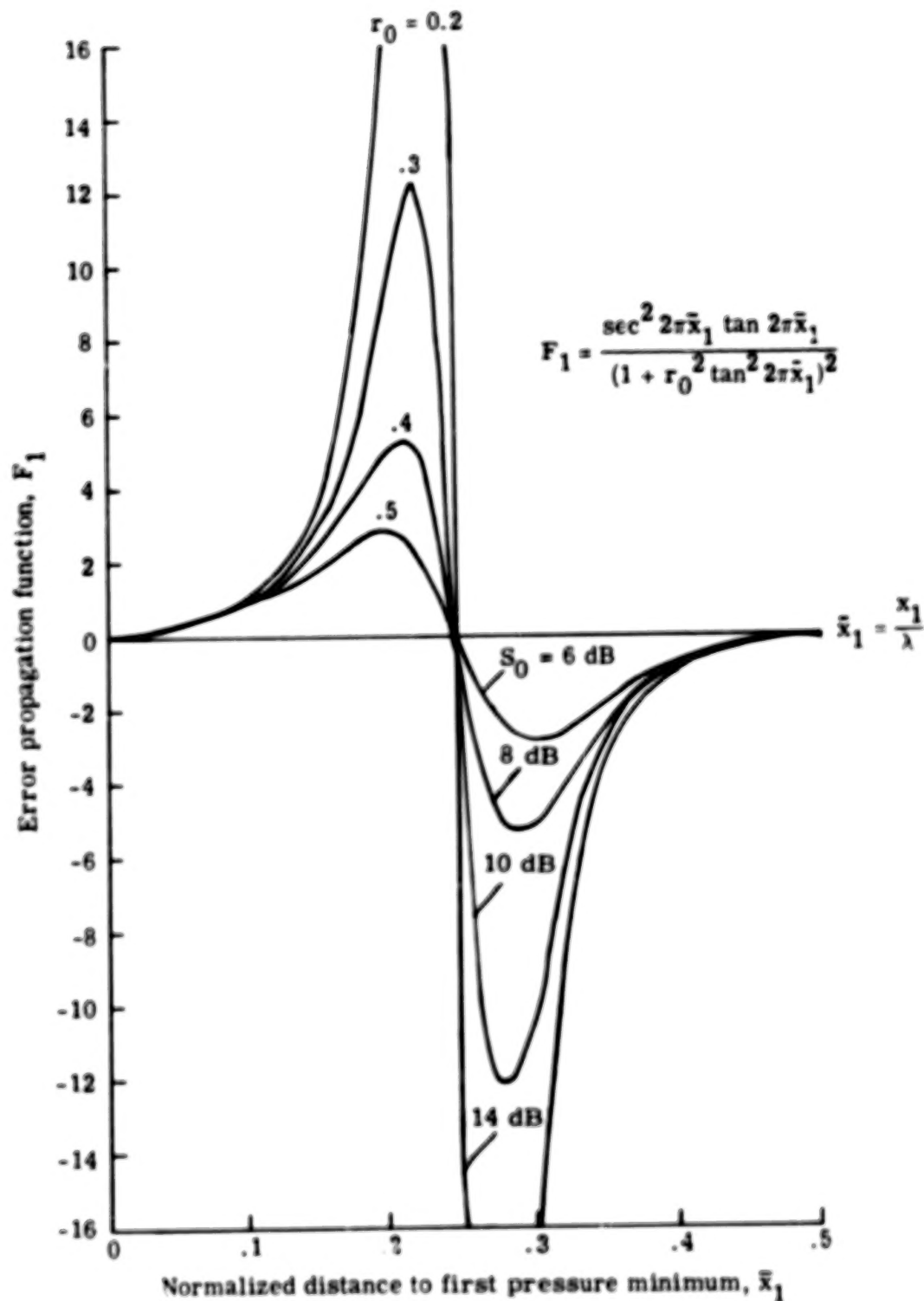
Figure 9.- Error propagation function F_1 plotted against distance to first pressure minimum in wavelengths with reciprocal standing-wave ratio r_0 as parameter.

48.

$$F_2 = \frac{\sec^2 2\pi \bar{x}_1 (1 - r_0^2 \tan^2 2\pi \bar{x}_1)}{(1 + r_0^2 \tan^2 2\pi \bar{x}_1)^2}$$

$\bar{x}_1 = \dfrac{x_1}{\lambda}$

$r_0 = 0.2$

Normalized distance to first pressure minimum, $\bar{x}_1$
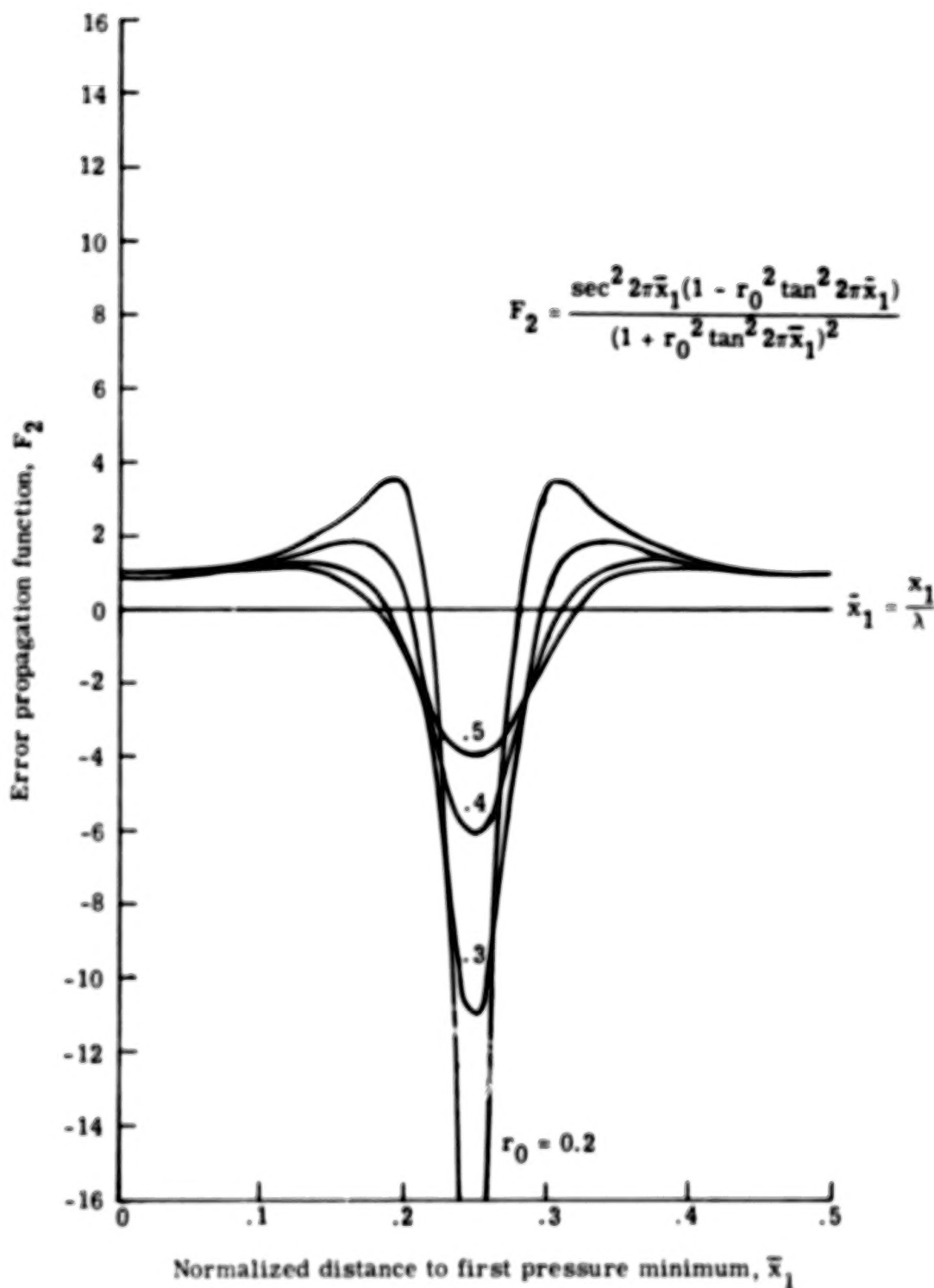
Figure 10.- Error propagation function F_2 plotted against distance to first pressure minimum in wavelengths with reciprocal standing-wave ratio r_0 as parameter.
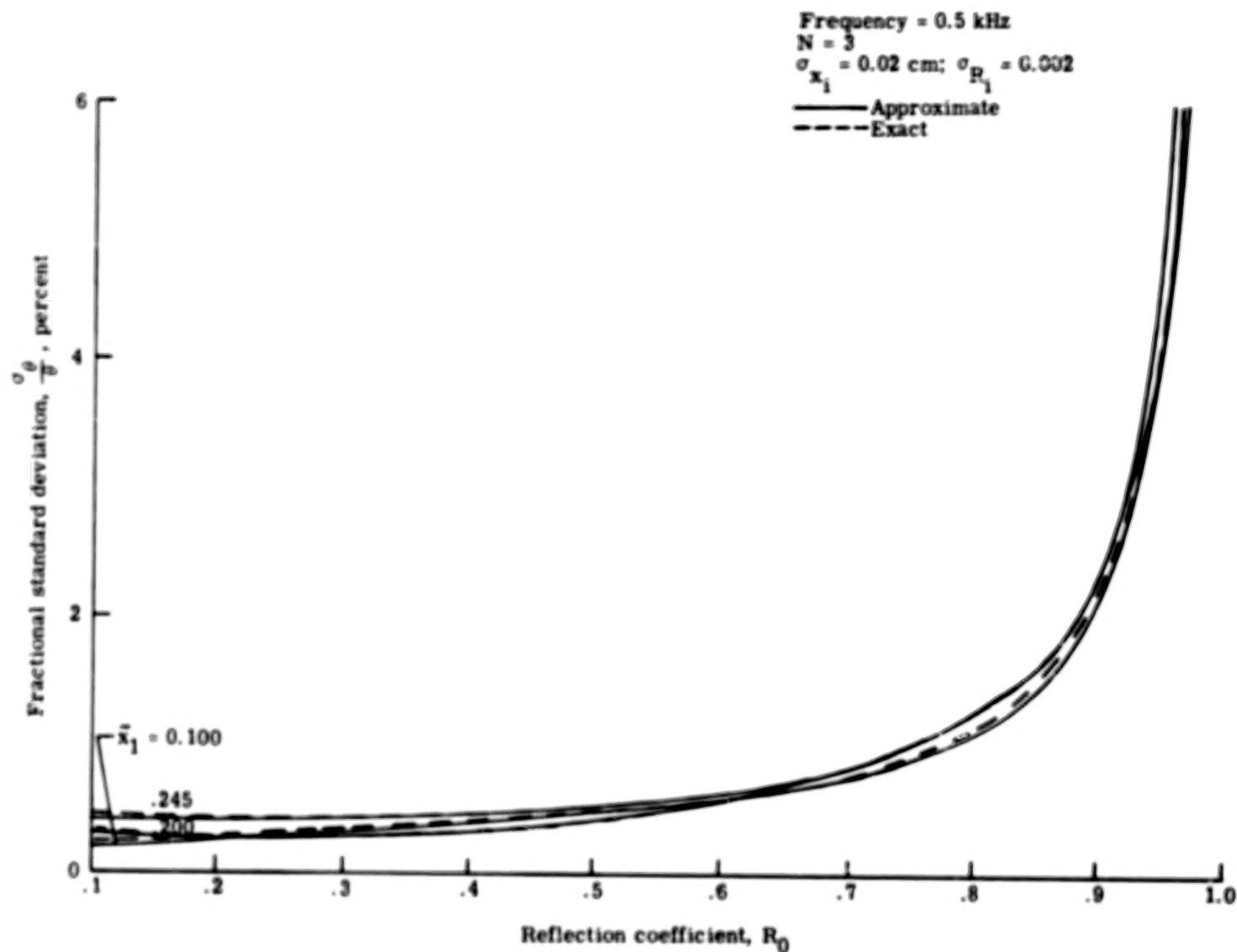
(a) Resistance ratio.

Figure 11.- Fractional standard deviation in impedance ratio components plotted against reflection coefficient with distance to first pressure minimum as parameter for frequency of 0.5 kHz.
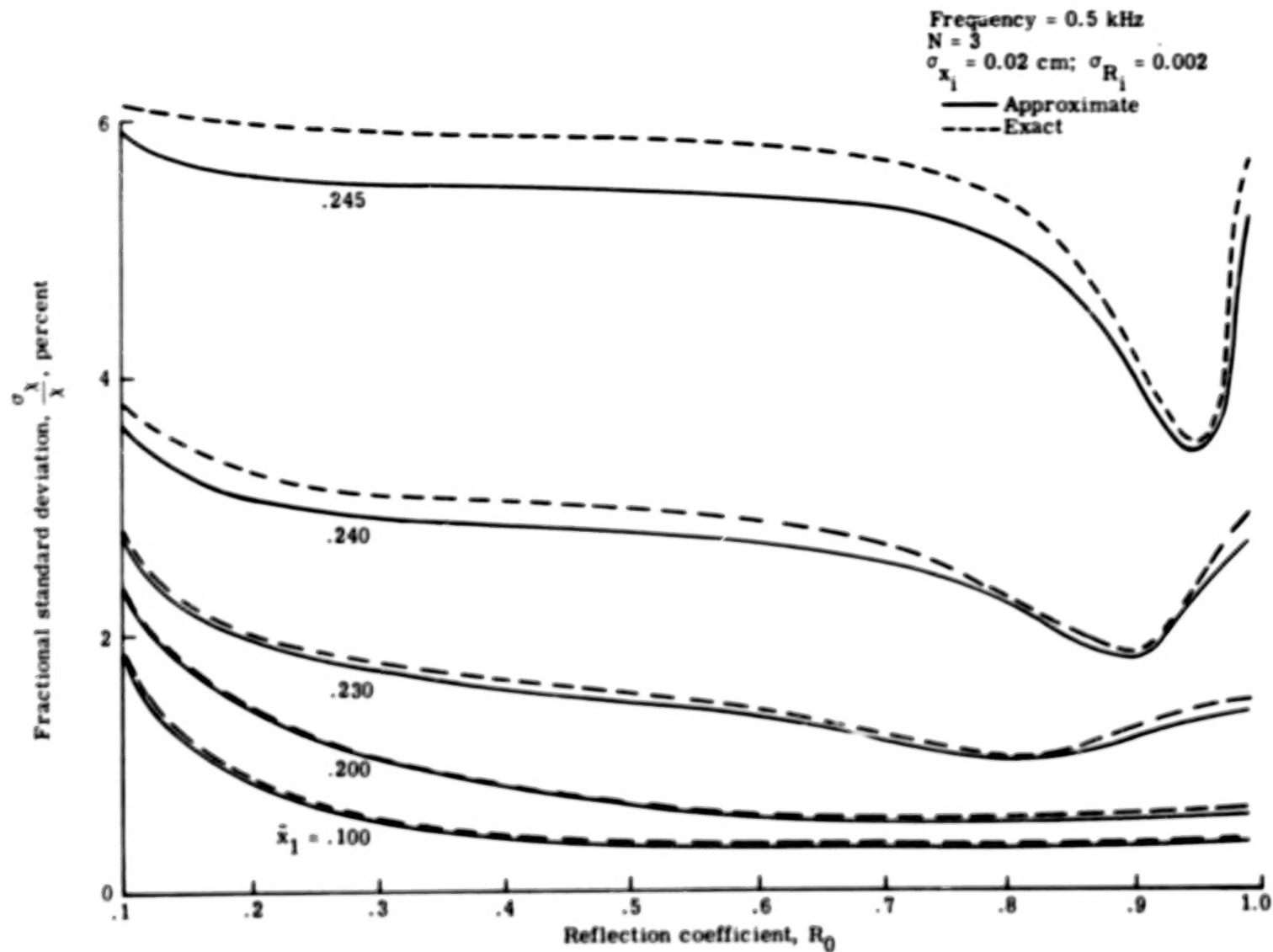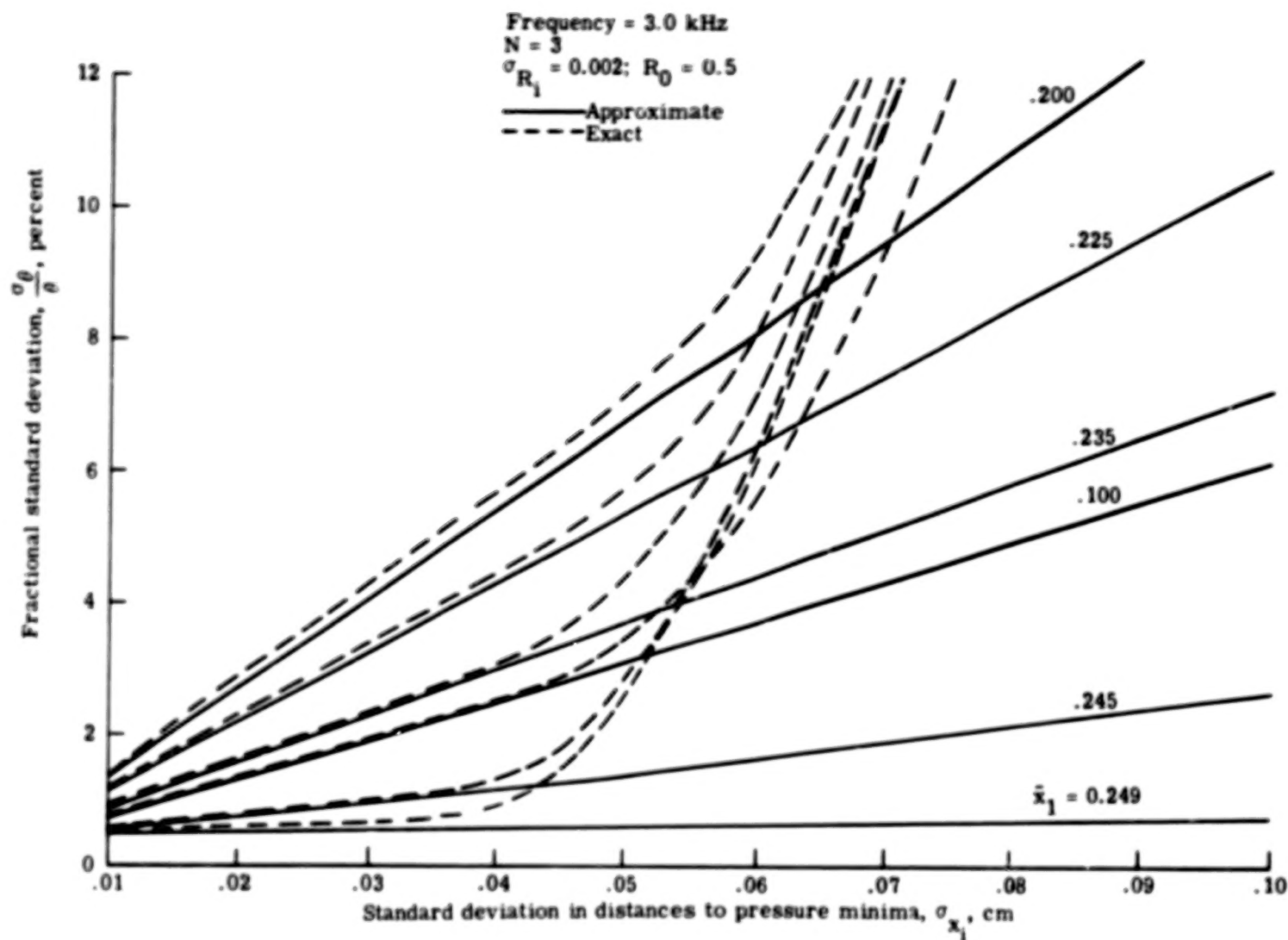
(b) Reactance ratio.
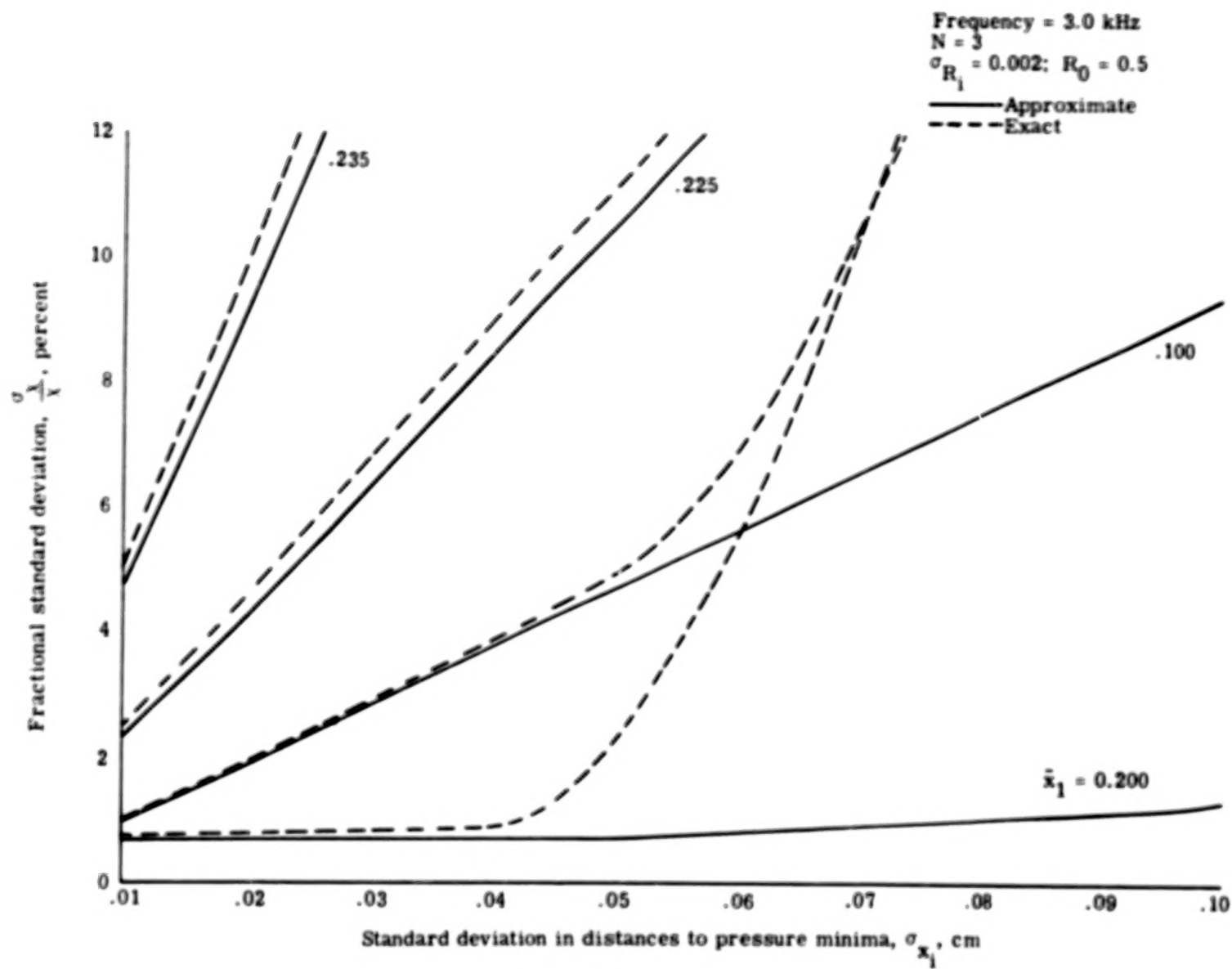
Figure 11.- Concluded.

51
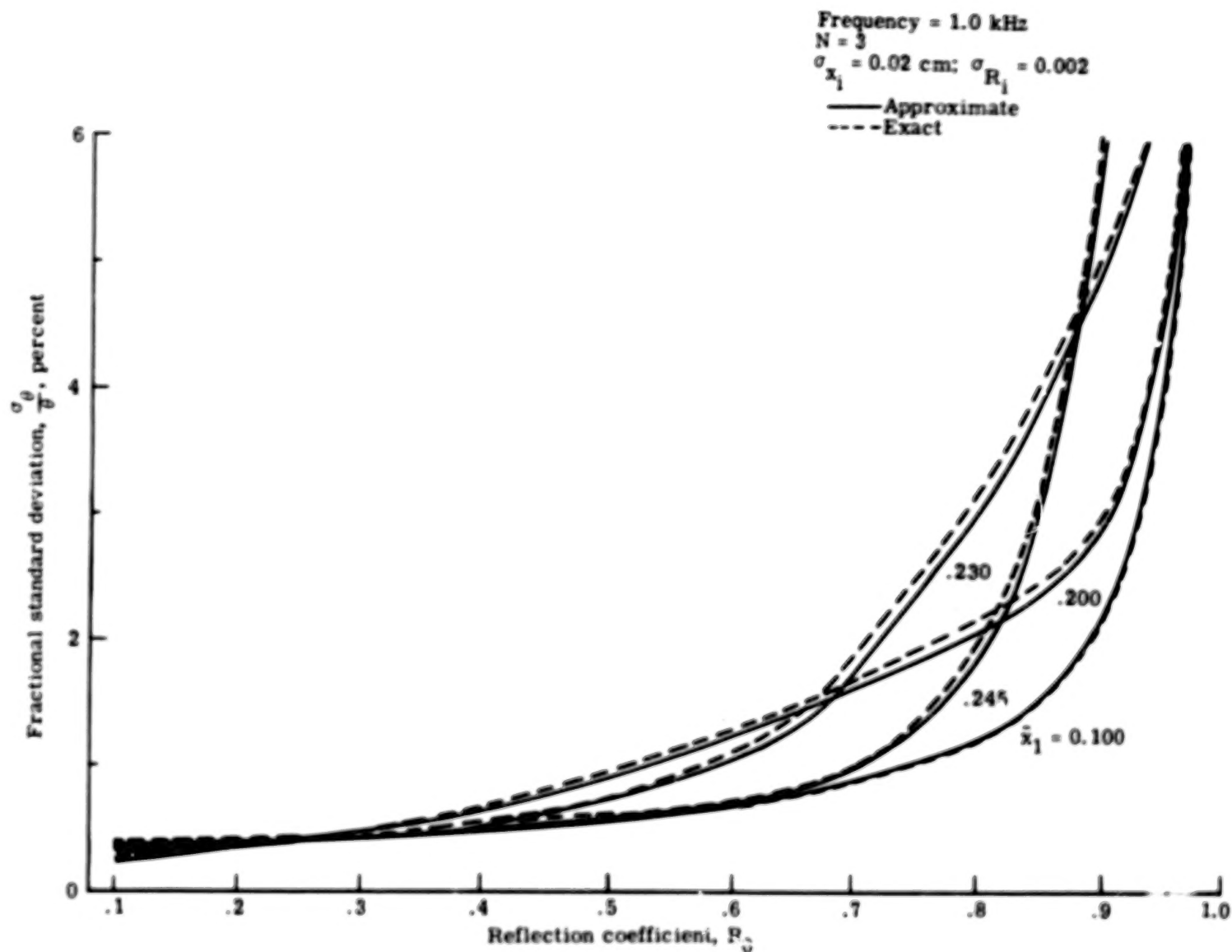
(a) Resistance ratio.

Figure 12.- Fractional standard deviation in impedance ratio components plotted against reflection coefficient with distance to first pressure minimum as parameter for frequency of 1.0 kHz.

52
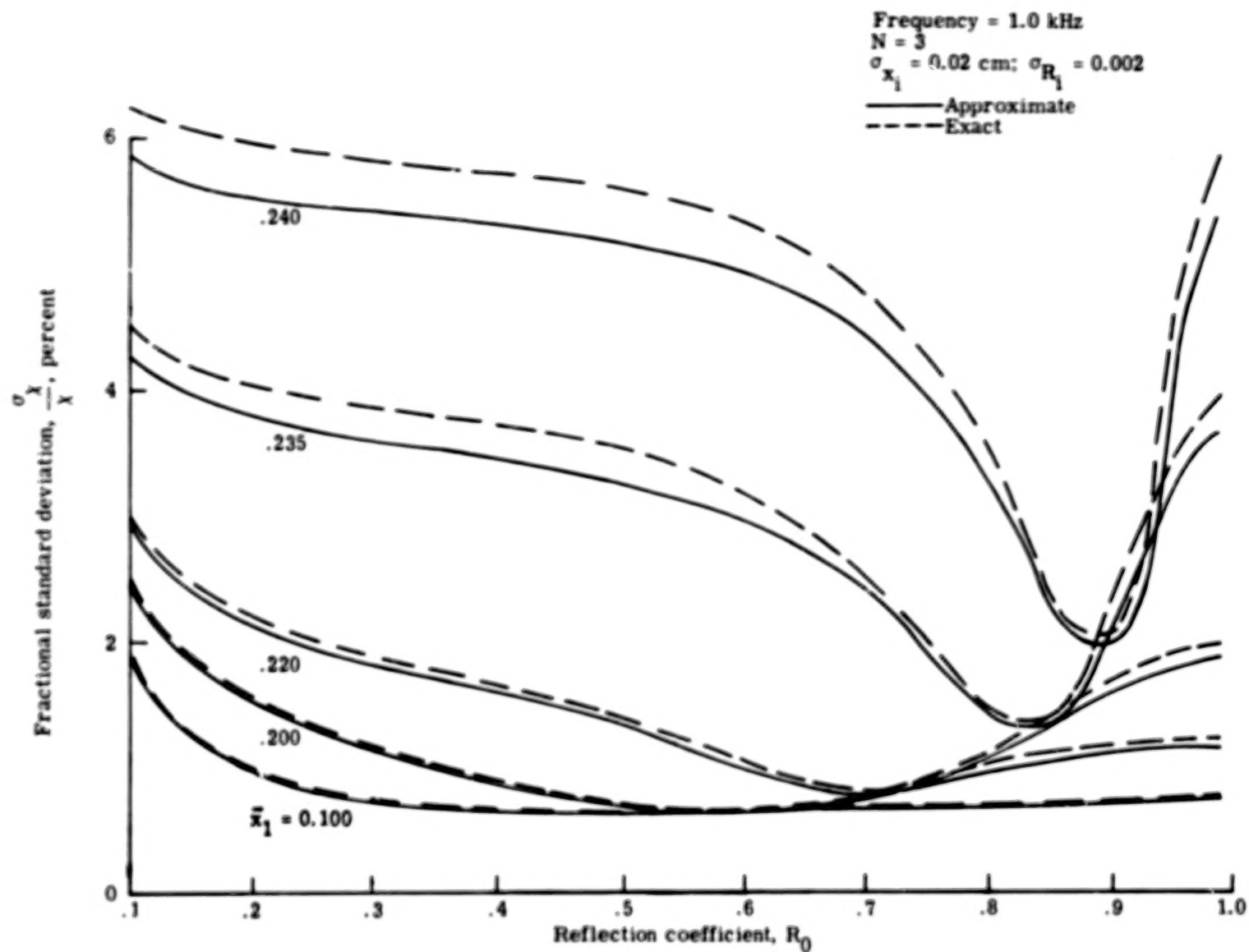
(b) Reactance ratio.

Figure 12.- Concluded.

53.

Frequency = 2.0 kHz
N = 3
$\sigma_{x_i} = 0.02$ cm; $\sigma_{R_i} = 0.002$

——— Approximate
— — — Exact

.225

.200

.245

$\bar{x}_1 = 0.100$

Fractional standard deviation, $\frac{\sigma_\theta}{\theta}$, percent

Reflection coefficient, R_0
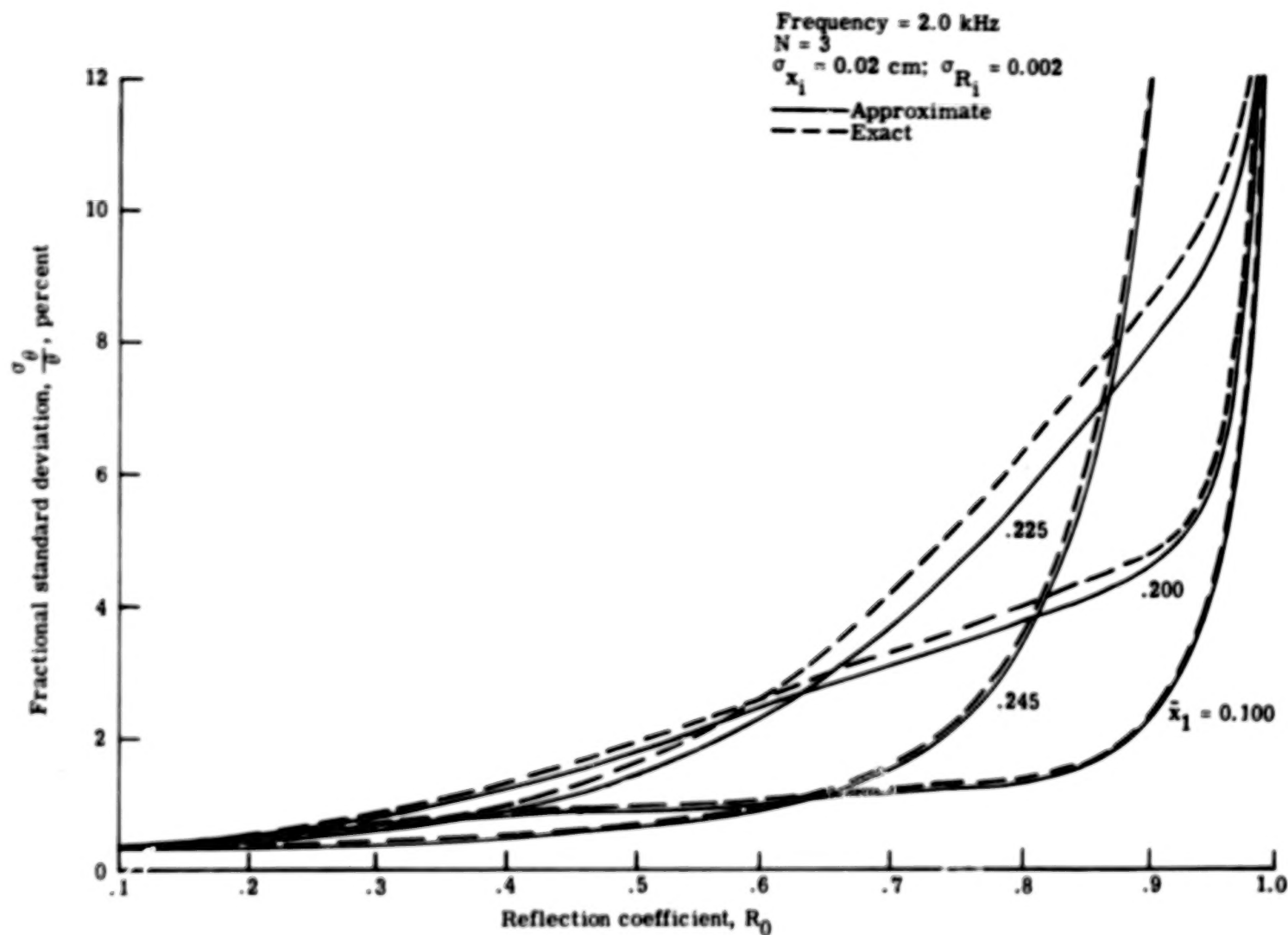
(a) Resistance ratio.

Figure 13.- Fractional standard deviation in impedance ratio components plotted against reflection coefficient with distance to first pressure minimum as parameter for frequency of 2.0 kHz.

54.

Frequency = 2.0 kHz
N = 3
$\sigma_{x_i} = 0.02$ cm; $\sigma_{R_i} = 0.002$
————— Approximate
– – – – Exact
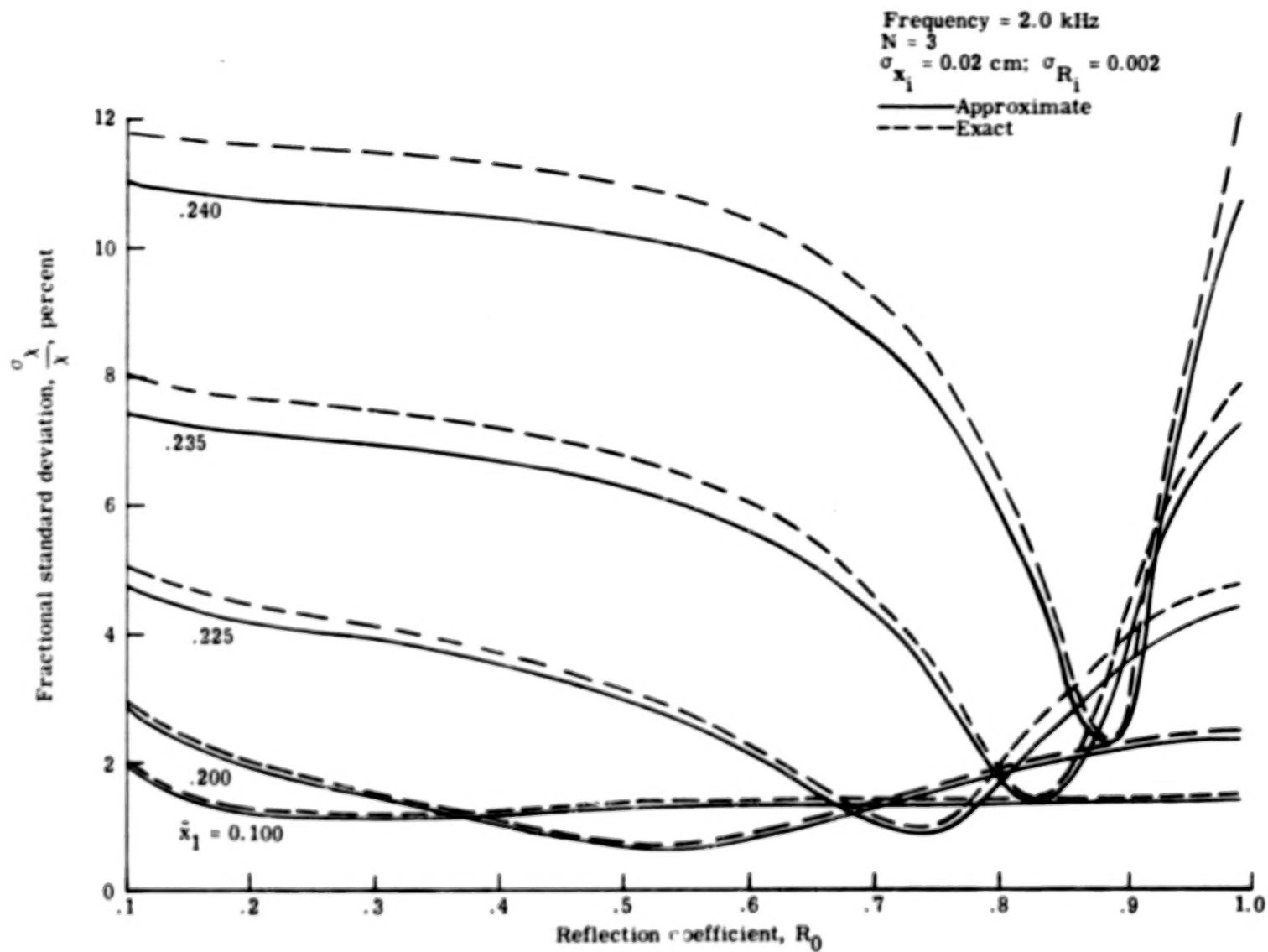
(b) Reactance ratio.

Figure 13.- Concluded.

55.
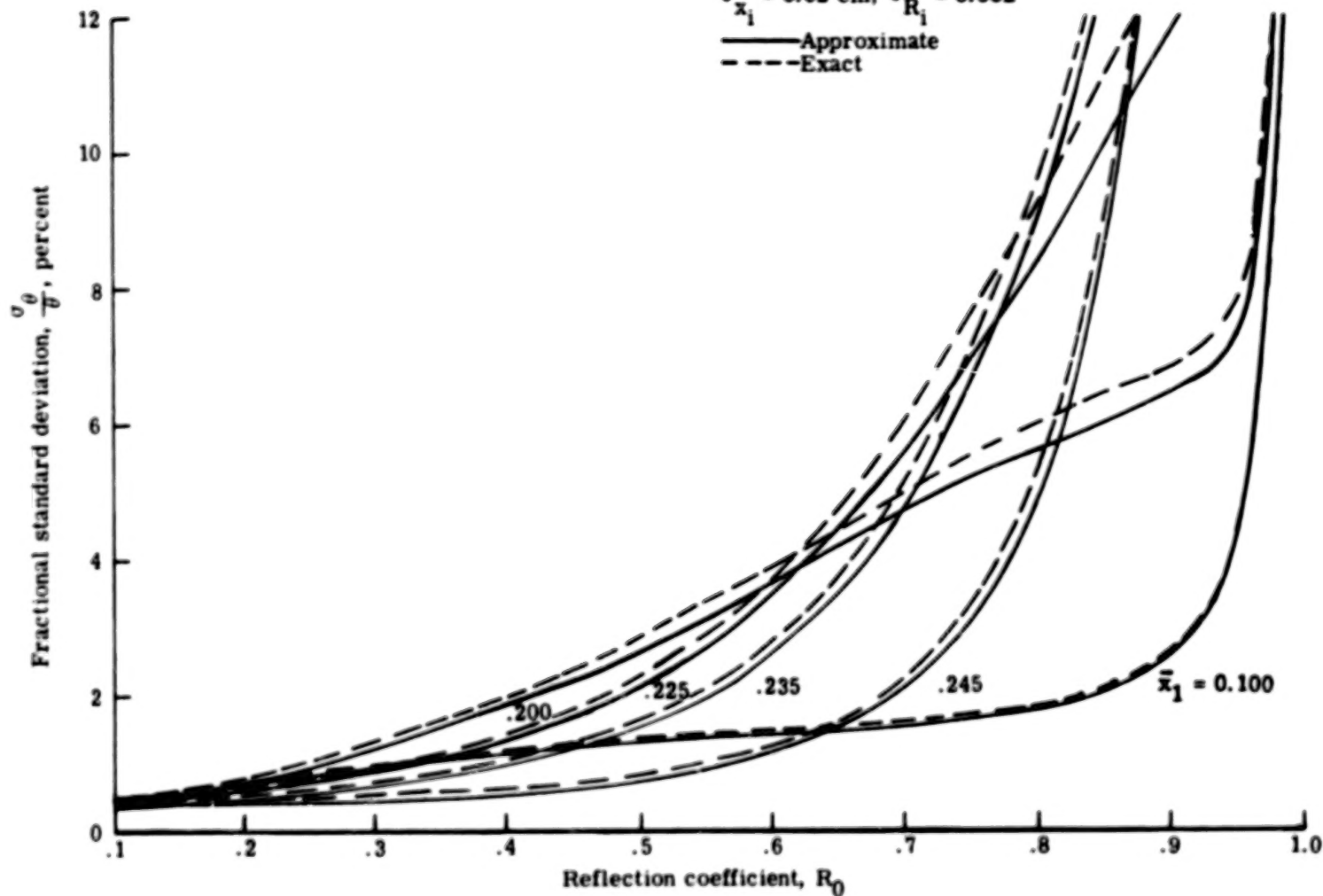
Figure 14.- Fractional standard deviation in impedance ratio components plotted against reflection coefficient with distance to first pressure minimum as parameter for frequency of 3.0 kHz.

(a) Resistance ratio.

56.

Frequency = 3.0 kHz
N = 3
σ_{x_i} = 0.02 cm; σ_{R_i} = 0.002
——— Approximate
- - - Exact
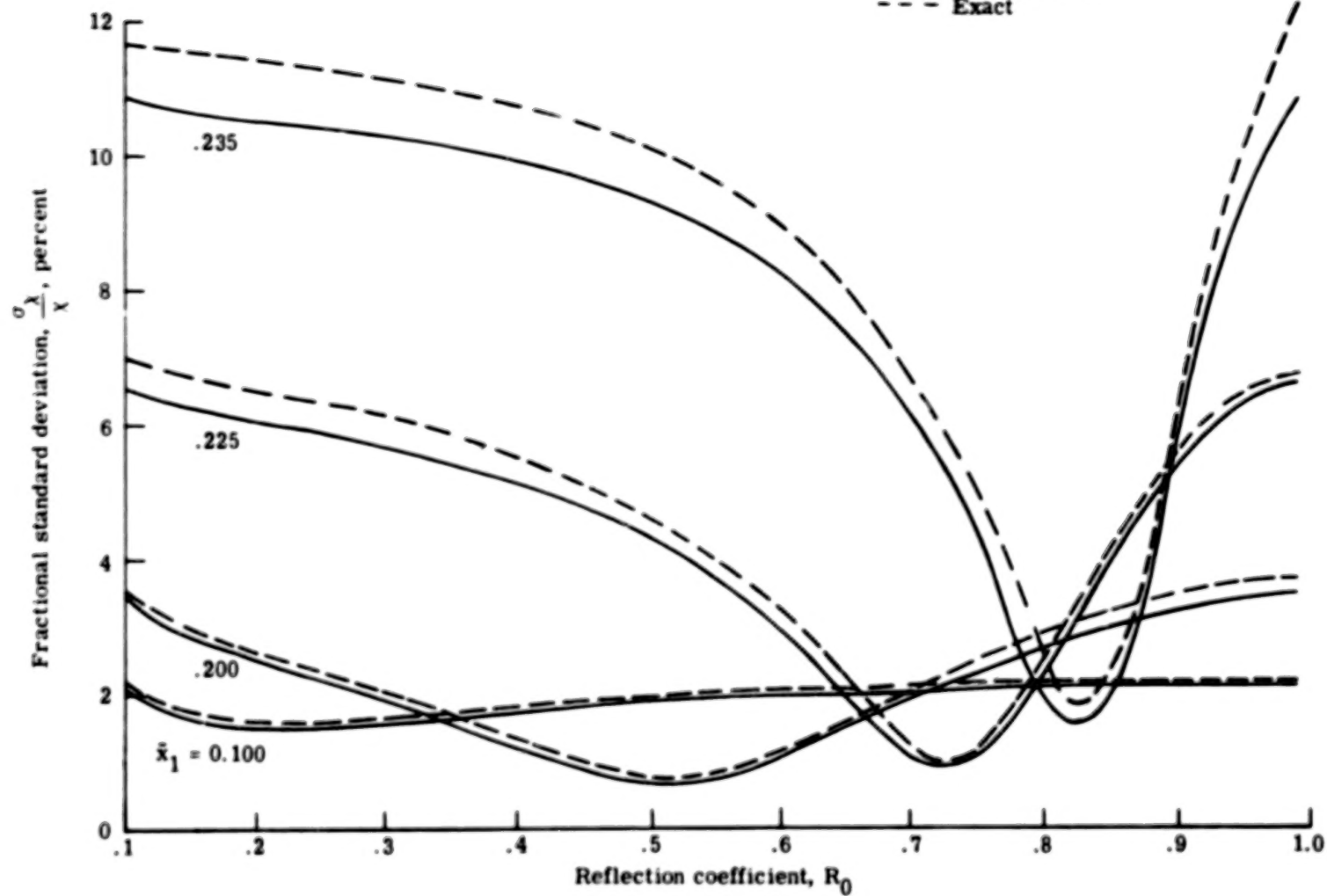
(b) Reactance ratio.

Figure 14.- Concluded.

57.
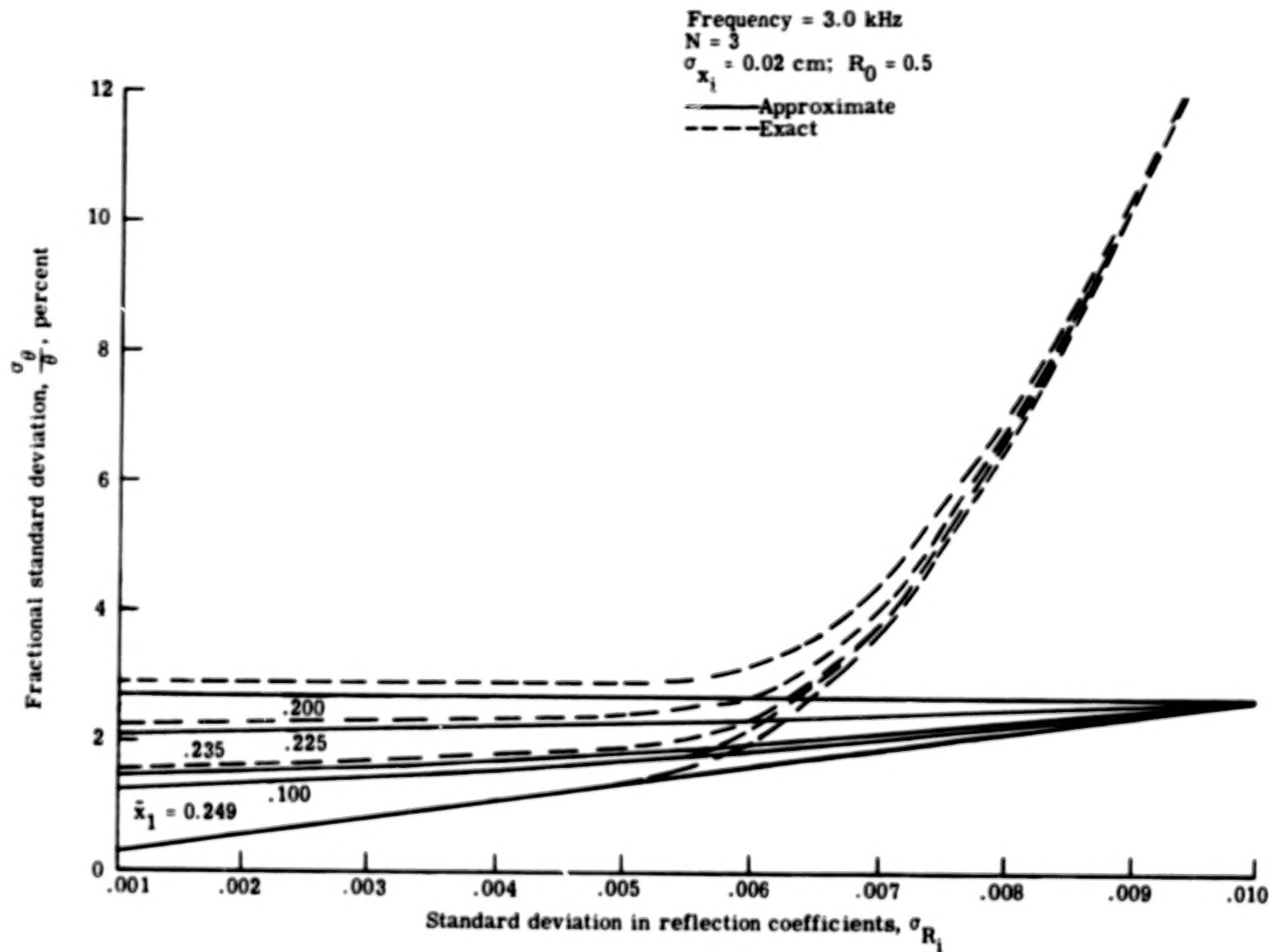
(a) Resistance ratio.

Figure 15.- Fractional standard deviation in impedance ratio components plotted against
standard deviation in reflection coefficients with distance to first pressure minimum
as parameter.

Frequency = 3.0 kHz
N = 3
$\sigma_{x_i} = 0.02$ cm; $R_0 = 0.5$
——— Approximate
— — — Exact
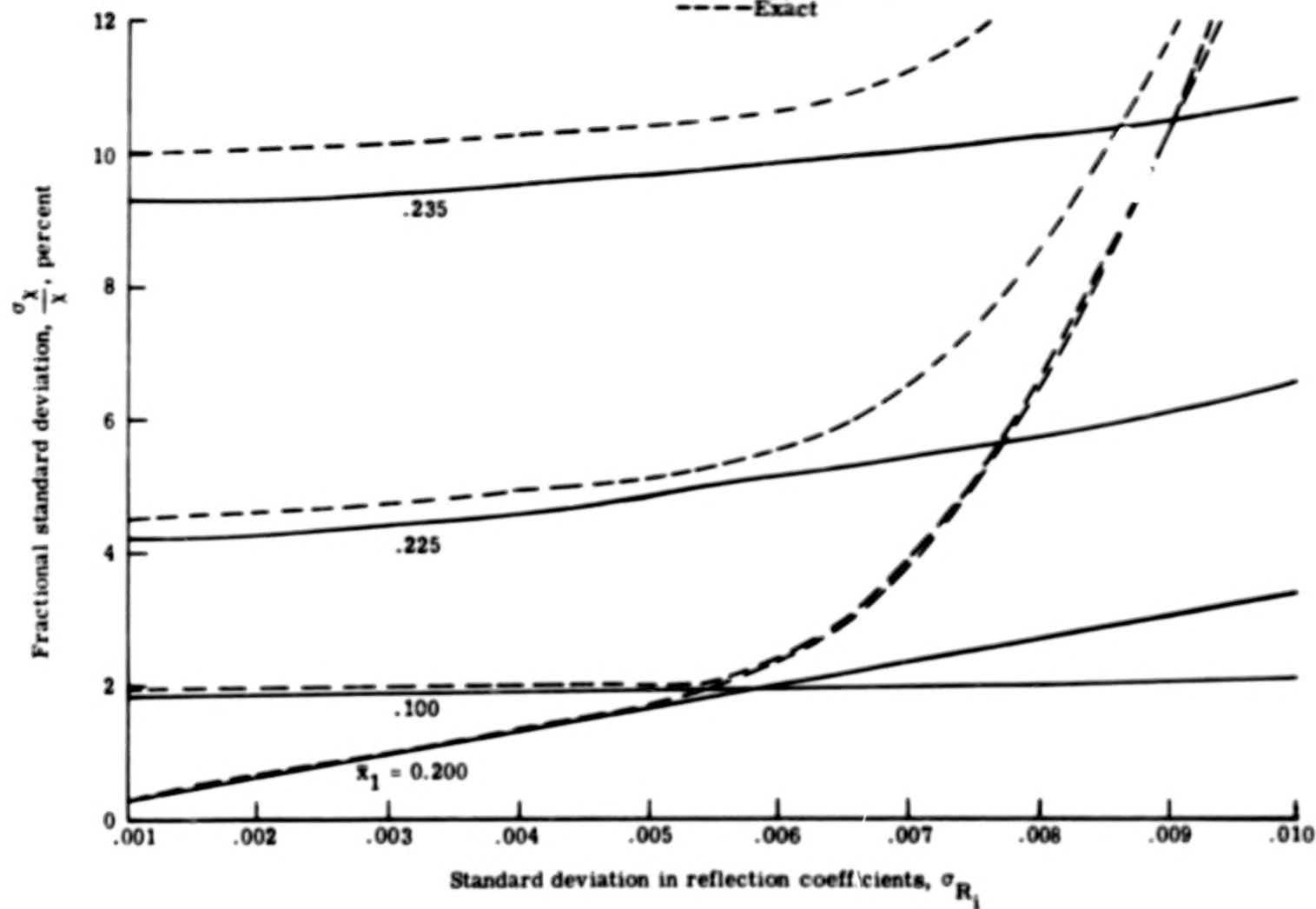
(b) Reactance ratio.

Figure 15.- Concluded.

59.

(a) Resistance ratio.

Figure 16.- Fractional standard deviation in impedance ratio components plotted against standard deviation in distances to pressure minima with distance to first pressure minimum as parameter.

60.

(b) Reactance ratio.

Figure 16.- Concluded.

61
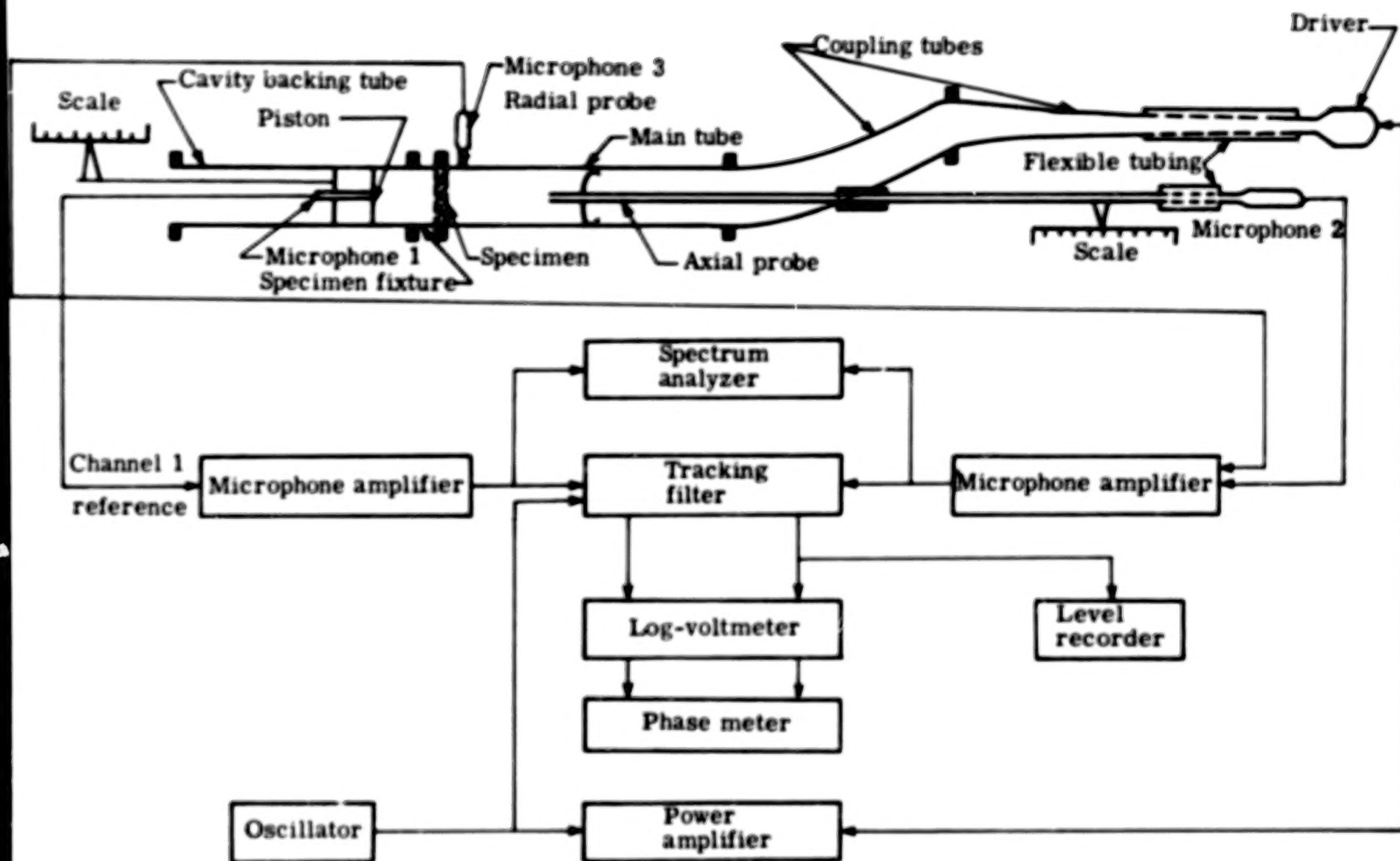
Figure 17.- Block diagram of experimental setup.

62.
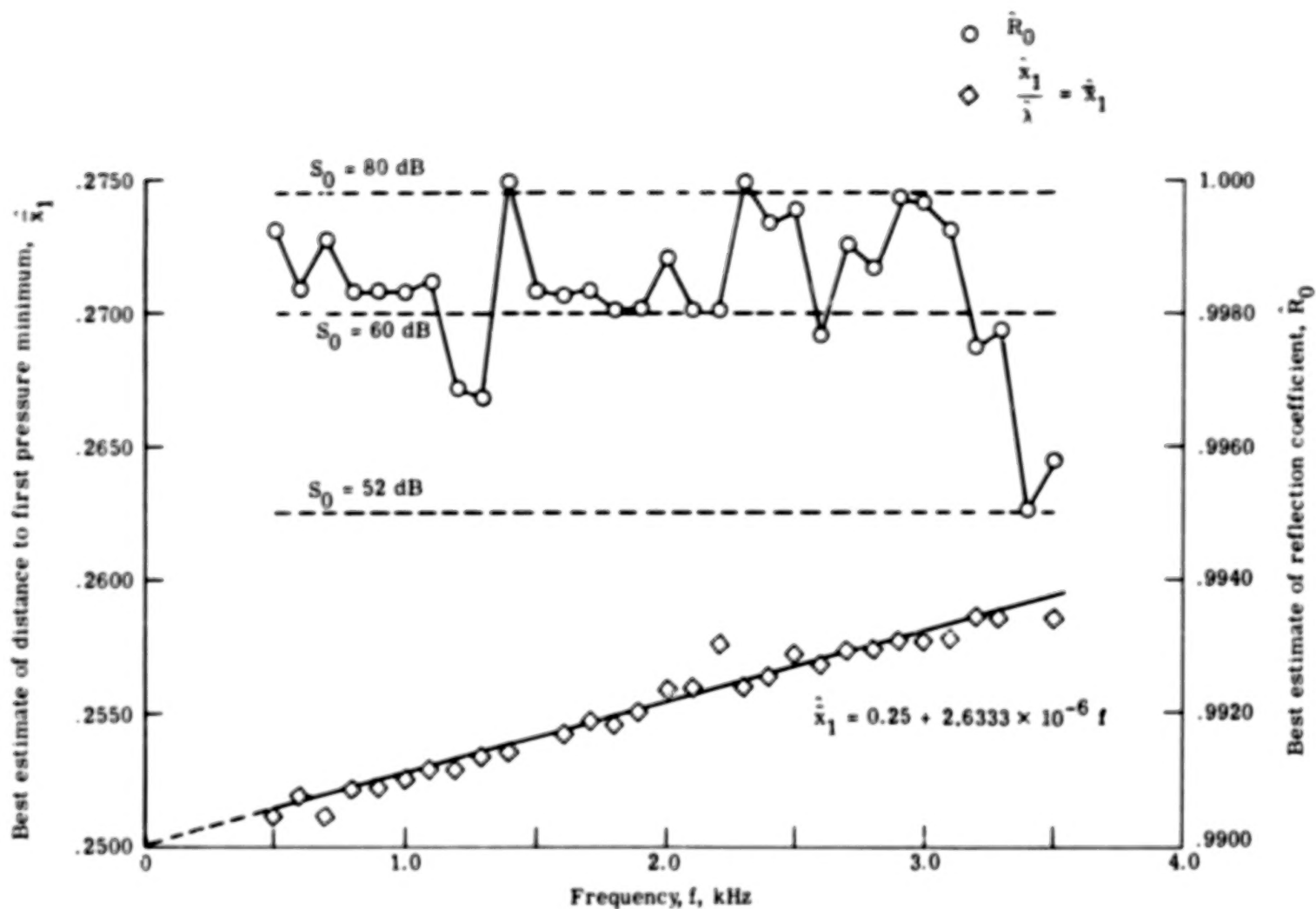
Figure 18.- Best estimate of distance to first pressure minimum and best estimate of reflection coefficient plotted against frequency for "rigid" piston.

63
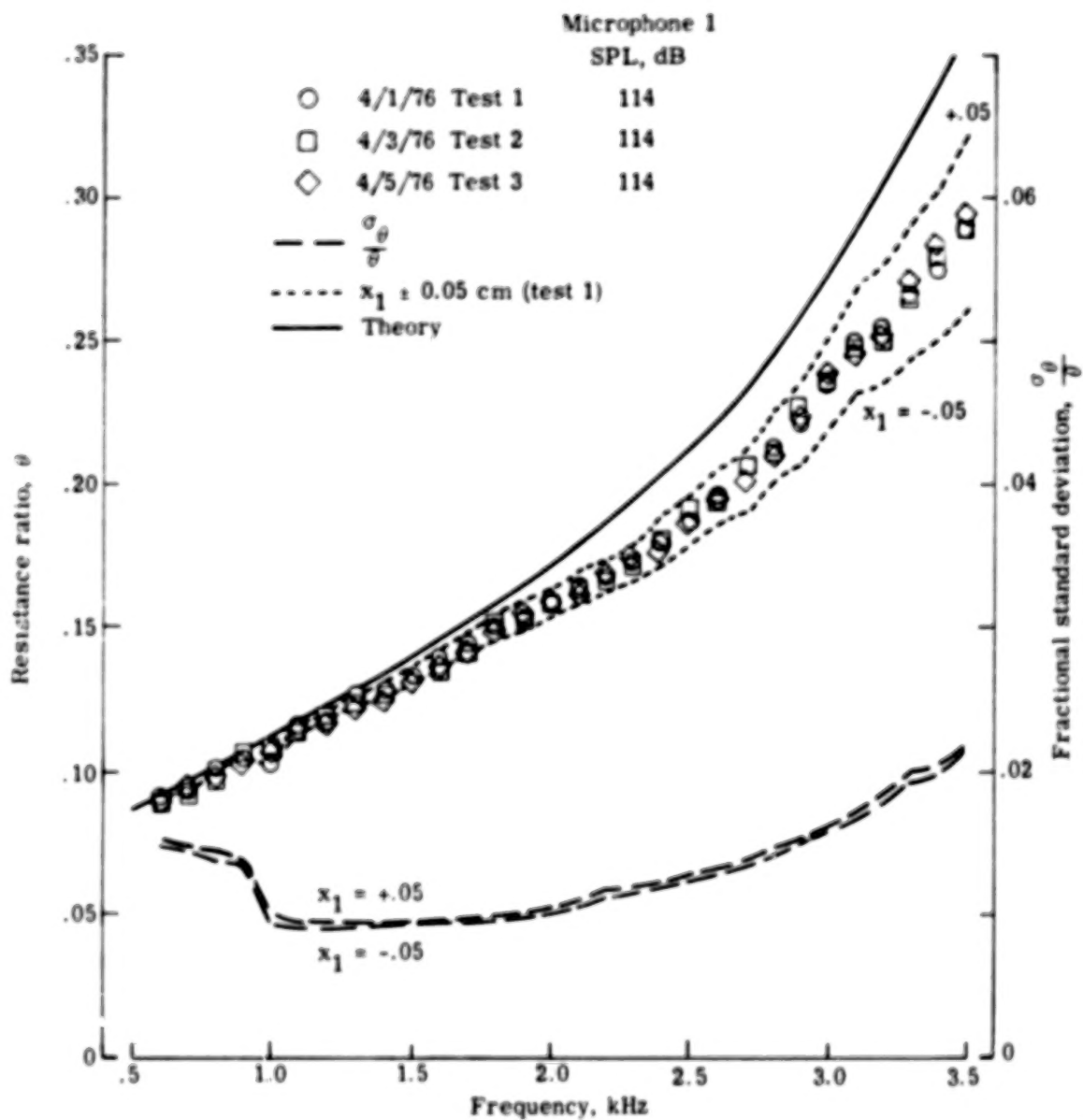
Figure 19.- Resistance ratio plotted against frequency for specimen A.

64.
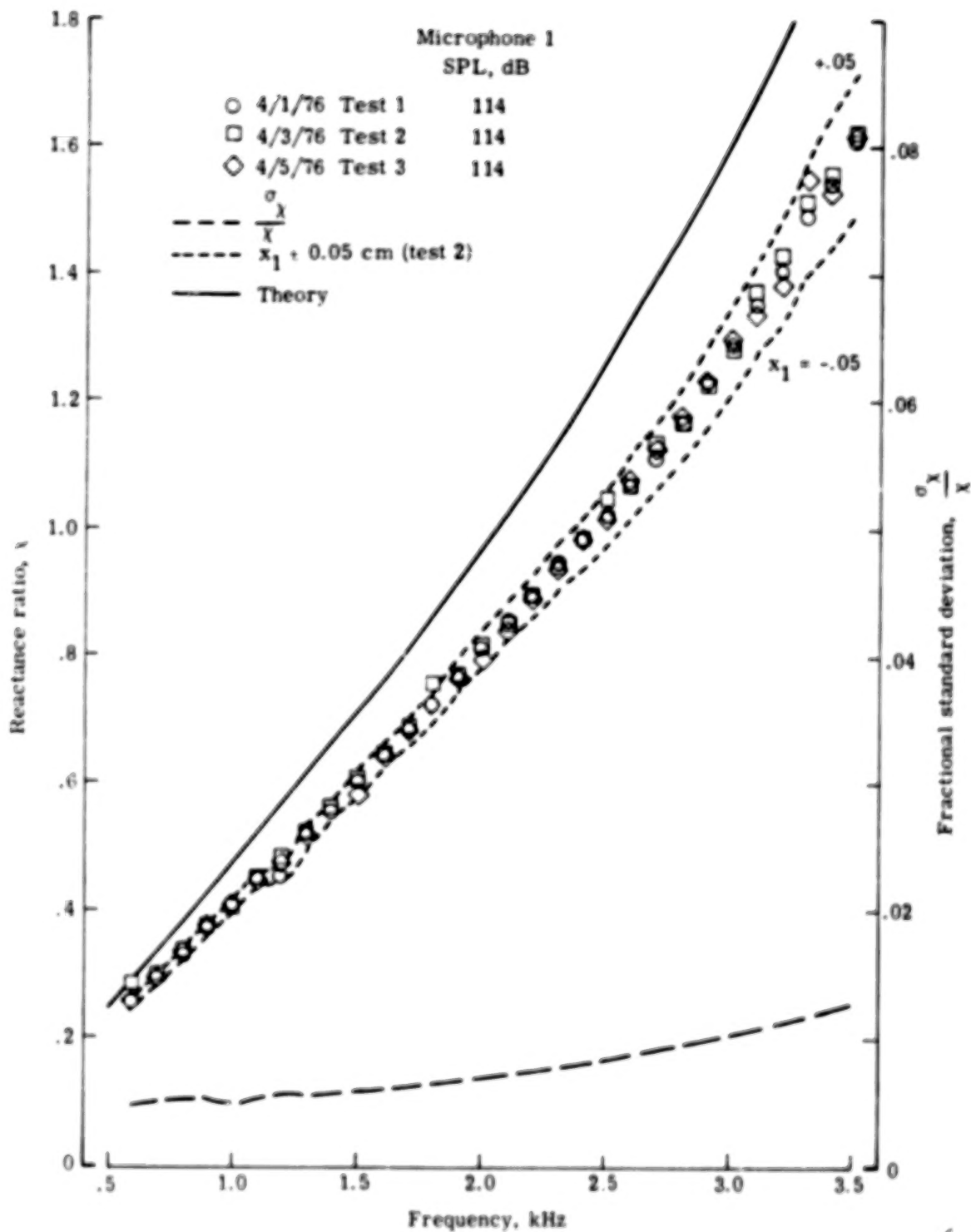
Figure 20.- Reactance ratio plotted against frequency for specimen A.
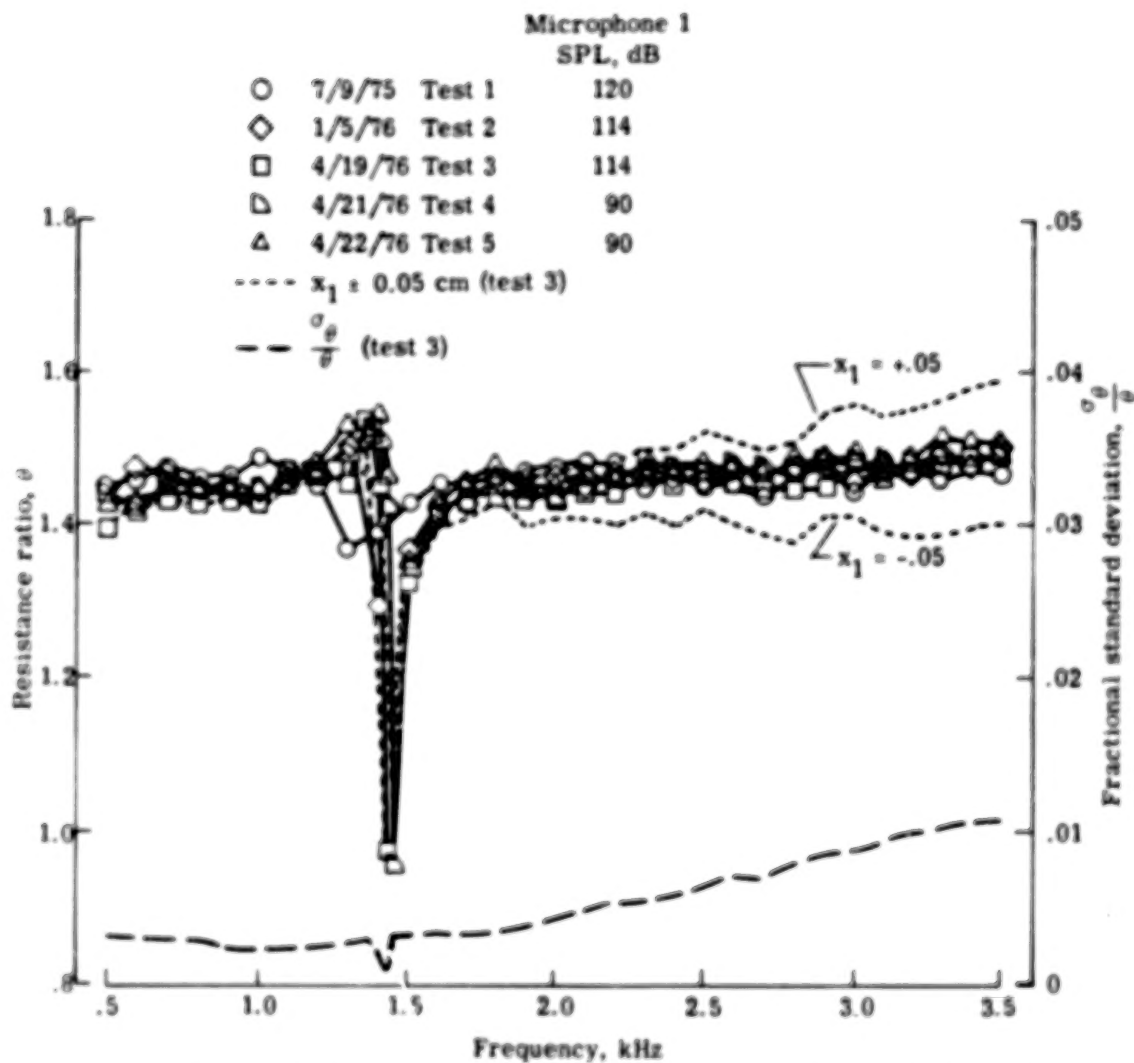
Figure 21.- Resistance ratio plotted against frequency for specimen B.
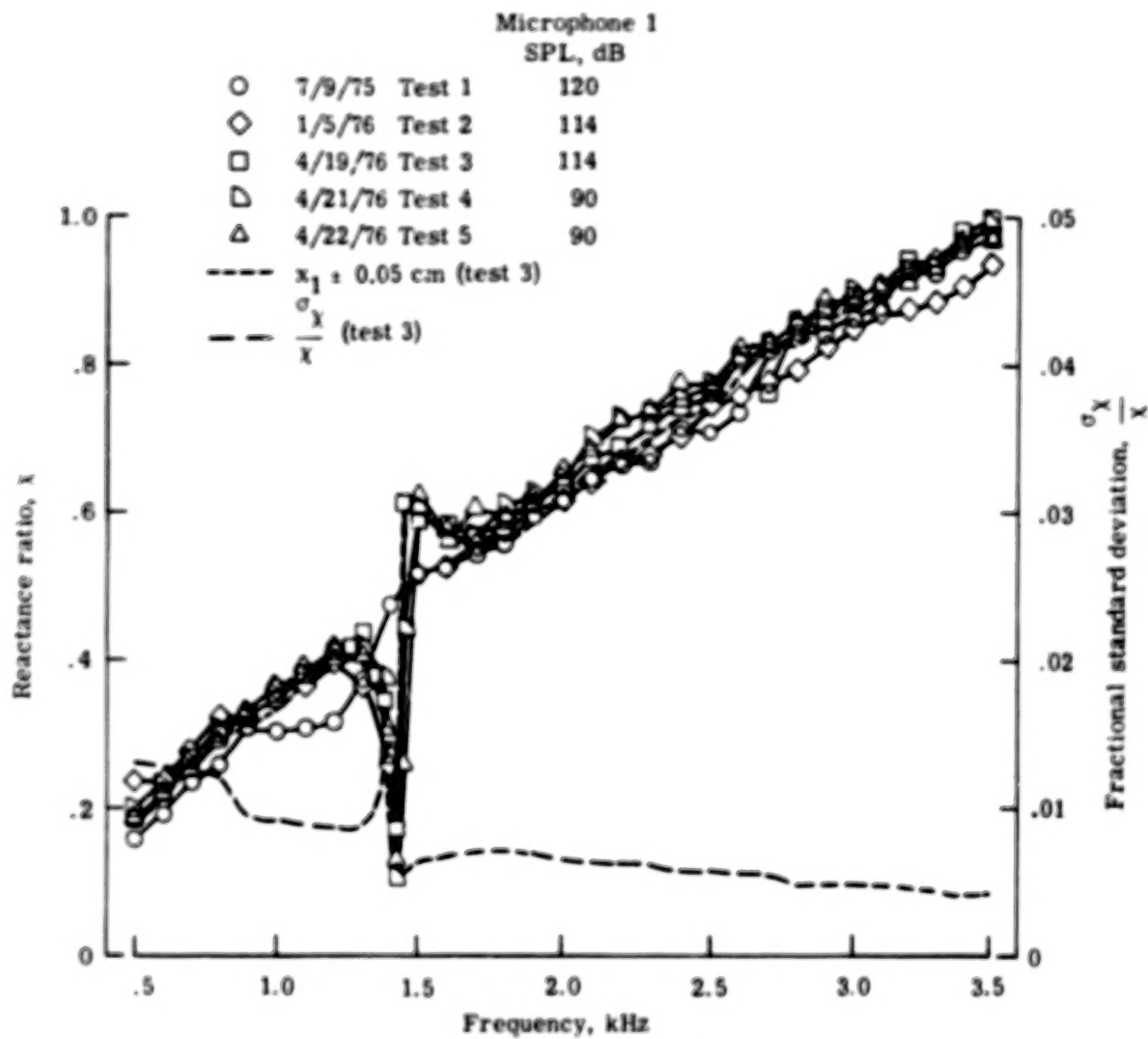
Figure 22.- Reactance ratio plotted against frequency for specimen B.

67
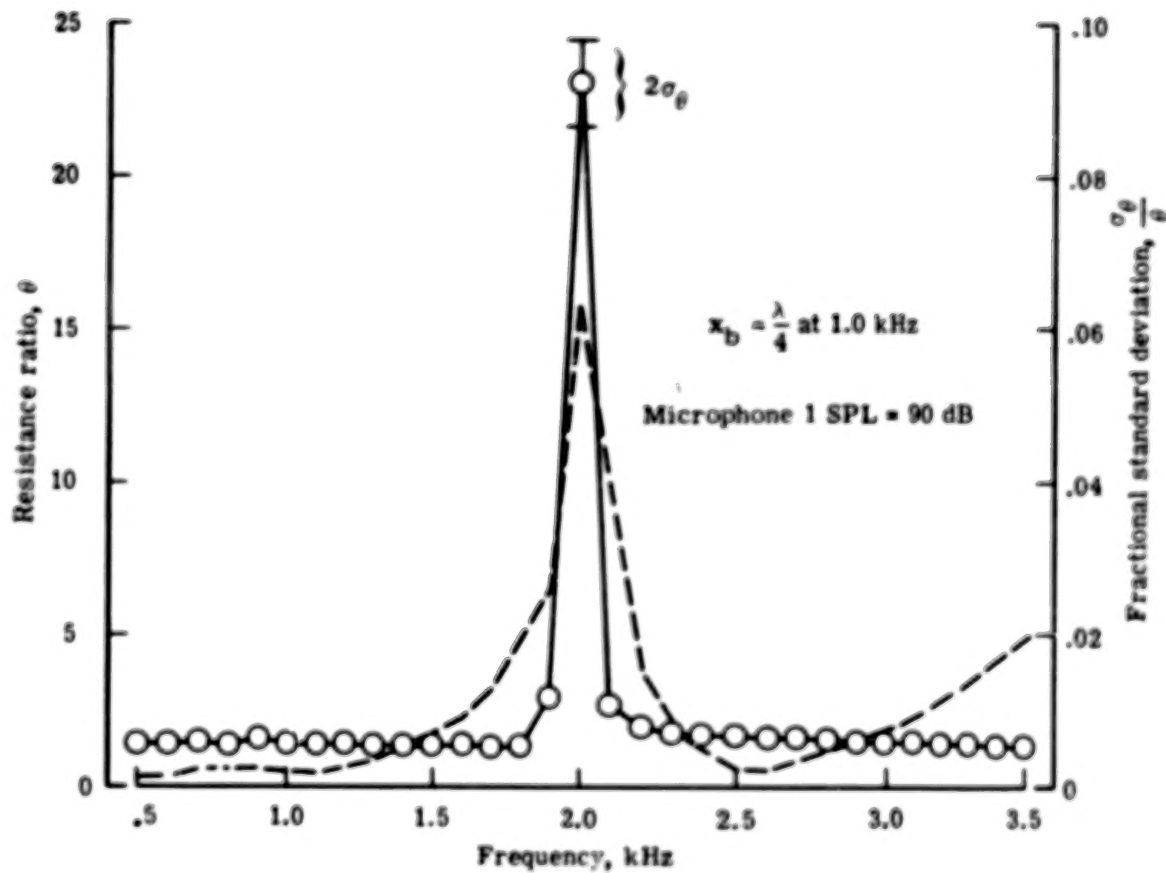
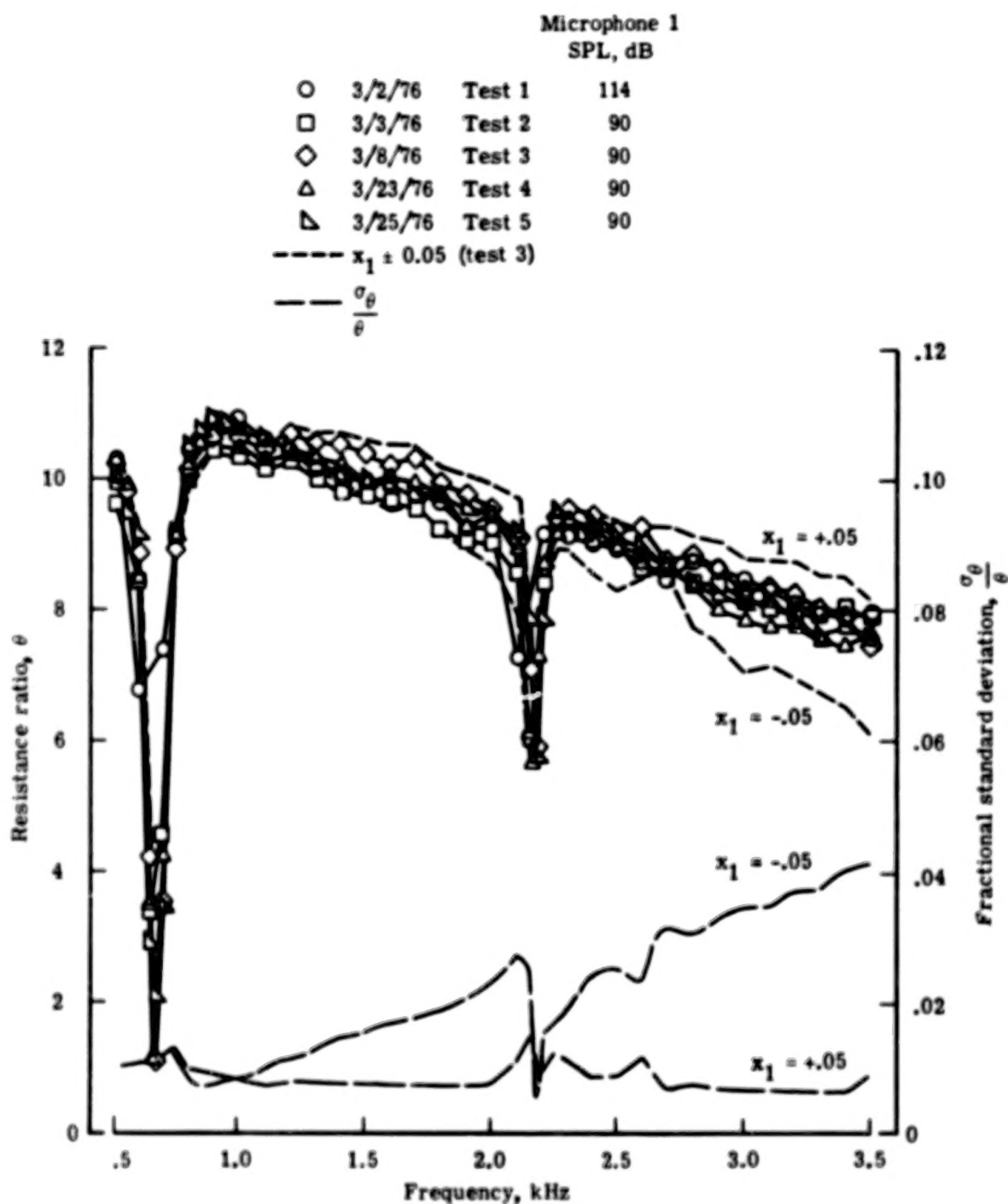Figure 23.- Resistance ratio for specimen B plotted against frequency for constant cavity depth.
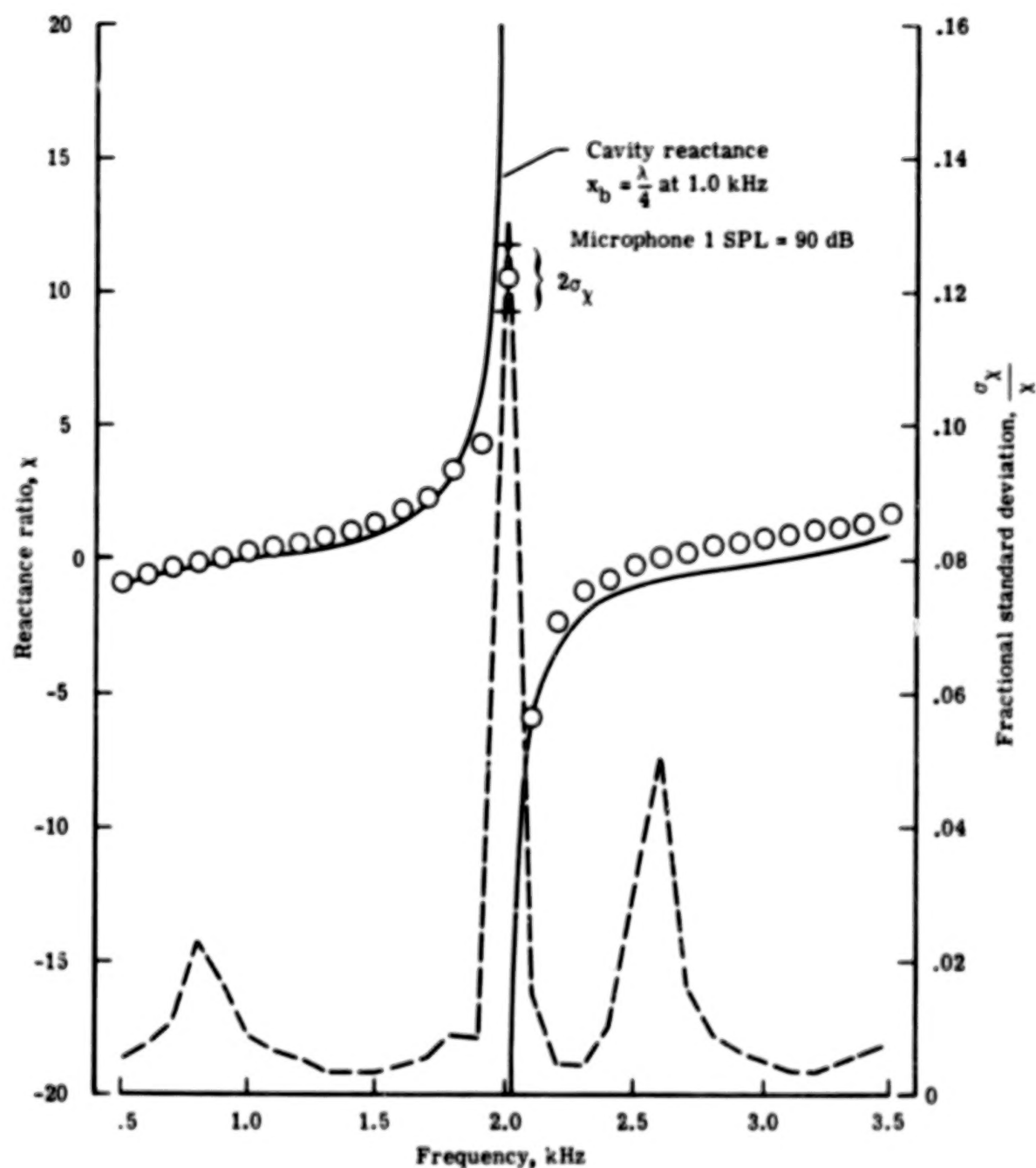
Figure 24.- Reactance ratio for specimen B plotted against frequency for constant cavity depth.

Figure 25.- Resistance ratio plotted against frequency for specimen C.
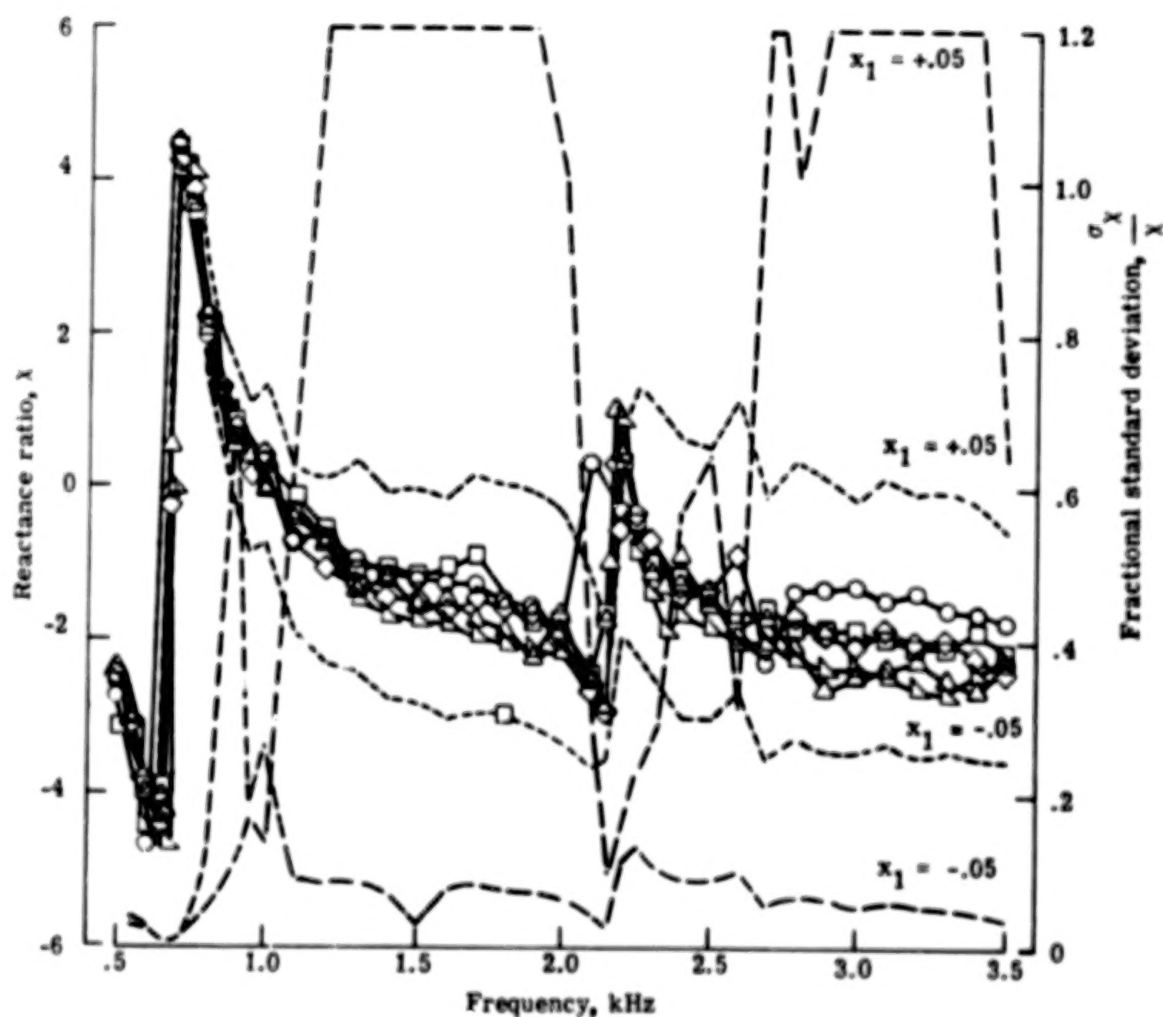
Figure 26.- Reactance ratio plotted against frequency for specimen C.

90

80

END

5.19 78